



## ARCHIVIO ISTITUZIONALE DELLA RICERCA

### Alma Mater Studiorum Università di Bologna Archivio istituzionale della ricerca

New Converter Solution with a Compact Modular Multilevel Structure Suitable for High-Power Medium-Voltage Wind Turbines

This is the final peer-reviewed author's accepted manuscript (postprint) of the following publication:

*Published Version:*

New Converter Solution with a Compact Modular Multilevel Structure Suitable for High-Power Medium-Voltage Wind Turbines / Gontijo G.; Kerekes T.; Sera D.; Ricco M.; Mathe L.; Teodorescu R.. - In: IEEE TRANSACTIONS ON POWER ELECTRONICS. - ISSN 0885-8993. - ELETTRONICO. - 38:2(2023), pp. 2626-2645. [10.1109/TPEL.2022.3213142]

This version is available at: <https://hdl.handle.net/11585/899797> since: 2024-04-12

*Published:*

DOI: <http://doi.org/10.1109/TPEL.2022.3213142>

*Terms of use:*

Some rights reserved. The terms and conditions for the reuse of this version of the manuscript are specified in the publishing policy. For all terms of use and more information see the publisher's website.

(Article begins on next page)

This item was downloaded from IRIS Università di Bologna (<https://cris.unibo.it/>).  
When citing, please refer to the published version.

# New Converter Solution with a Compact Modular Multilevel Structure Suitable for High-Power Medium-Voltage Wind Turbines

Gustavo Gontijo, *Member, IEEE*, Tamas Kerekes, *Senior Member, IEEE*, Dezso Sera, *Senior Member, IEEE*, Mattia Ricco, *Senior Member, IEEE*, Laszlo Mathe, *Senior Member, IEEE*, and Remus Teodorescu, *Fellow, IEEE*

**Abstract**—Modern wind turbines with increasing power levels are continuously emerging. These power levels are reaching a point where excessively high currents are obtained if the traditional low-voltage wind-turbine structure is adopted. High currents lead to excessively high losses and the need for bulky and heavy conductors to carry them. A medium-voltage structure should be a more competitive alternative to be adopted in high-power wind turbines. In this paper, a new converter solution with a modular multilevel structure suitable for driving modern/future high-power medium-voltage wind turbines is proposed. This converter topology has desirable features common to modular multilevel converters such as the improved reliability at high voltage levels, and the possibility to synthesize high-power-quality staircase-shape voltages, which leads to low requirements for harmonic and  $\frac{dv}{dt}$  filters. Furthermore, the proposed converter presents reduced capacitance and inductance requirements compared to other well-established modular multilevel converter topologies, which should result in a lighter and more compact solution. The proposed solution could potentially allow for the reduction of the overall costs of the supporting structure required to withstand the weight of the wind turbine. Simulation and experimental results are presented in this paper to validate the proposed topology.

**Index Terms**—modular multilevel converters, wind turbines.

## I. INTRODUCTION

WITH the increasing development of engineering and technology, wind turbines (WTs) with higher power ratings are continuously emerging. If the traditional low voltage structure (including generator, power-electronic converter, etc.) is adopted, then excessively high currents will flow through the modern WTs, leading to undesirably high losses and to the necessity of heavy and bulky conductors to carry such currents [1], [2]. Adopting a medium-voltage structure can considerably reduce the current levels of the WTs resulting in more cost-effective solutions [3]–[5]. Besides, with the increased voltage ratings, the size of the turbine transformer can be reduced and even a transformer-less unit could eventually be built [6].

The two-level (TL) three-phase converter is the standard solution for low-voltage applications. This topology presents simple structure and control and it is capable to synthesize voltages with high-order harmonics, that can easily be filtered out, when operating with high switching frequencies. However, the usage of TL converters in applications with higher voltage levels can be highly undesirable. To reach higher voltages using the semiconductor devices that are currently available in the industry, stacks built with series-connected devices might

be required. Problems related to static and dynamic voltage sharing among the series-connected devices can occur, which can make the system unsafe and unreliable [7]. These problems are more evident with increased switching frequencies. Snubber circuits could be adopted to avoid these problems but high losses would occur due to the high switching frequencies [7]. High switching frequencies also lead to high switching losses in the TL converter dealing with increased voltage and current levels. Another problem related to the operation of the TL converter in increased voltage levels is the high  $\frac{dv}{dt}$  imposed to the load (electrical machine) that can be harmful to its insulation [8]. Diode-clamped converters, such as the three-level neutral-point-clamped (NPC) converters, present improved performance in applications with increased voltages, and topologies with a higher number of levels can be built. Nonetheless, after a certain number of levels, diode-clamped converters become too complex to control and operate [8].

The modular multilevel converter (see Fig. 6 in Section IV) is the state-of-the art solution for high-power high-voltage applications that require a DC stage such as the high-voltage direct-current (HVDC) transmission systems [9]. The MMC is capable to reach high voltages without the need of series-connected semiconductor devices due to its modularity and scalability. Moreover, the MMC presents high reliability and the ability to synthesize a high-power-quality staircase-shape voltage. For these reasons, the MMC has also been proposed as an alternative for high-power electrical-machine drives, and it could be a suitable option to drive modern/future high-power medium-voltage WTs. Nonetheless, the MMC presents some drawbacks when driving electrical machines such as its intolerably high submodule-capacitor voltage ripple at low-frequency operation [10], [11]. Besides, due to its topology, with the presence of a DC stage, an undesirably large number of submodules is required. Each of these submodules has its own capacitor. These capacitors can be quite bulky, heavy and expensive, depending on the power level of the given application, which means that the MMC can be a quite bulky, heavy and expensive solution due to its large number of submodules [8].

In order to overcome some of the disadvantages of the MMC in machine-drive applications, new alternative converter topologies have been proposed in the literature, and one of the topologies that stands out the most is the so-called modular multilevel matrix converter (M<sup>3</sup>C) [6], [12], [13] also referred to as modular multilevel cascade converter based on triple-

star bridge-cells (MMCC-TSBC) [14]–[16]. The  $M^3C$  (see Fig. 7 in Section IV) presents improved performance at low-frequency operation, in comparison to the MMC, as it can be considered as an interesting solution to drive high-power electrical machines, especially in applications that require a low-frequency operation [12]. Moreover, the  $M^3C$  requires a reduced number of submodules, in comparison to the MMC, which translates into a reduced number of the heavy and bulky capacitors [12]. Nonetheless, the  $M^3C$  presents some drawbacks such as its extremely complex modulation and control, in which many internal control loops are required for the proper and stable operation of the converter [6], [14]–[16]. Besides, even though the  $M^3C$  presents a reduced submodule-capacitor voltage ripple at low frequencies, this ripple is increased the closer to the grid frequency the load-side frequency comes [12]. The  $M^3C$  presents an unstable behavior when its load-side frequency is equal to the grid-side frequency [12]. In WT applications specifically, the use of a  $M^3C$  might not be the best option (even though it has been considered in the literature for such application [2], [6], [12]) since in this case the generator is controlled to operate within a frequency range that does not include very low frequencies, but includes the nominal grid frequency (50/60 Hz). In other words, if the wind speed is below the cut-in speed, then the generator control is disabled, and the WT remains in parking mode [17]. The wind cut-in speed corresponds to a generator speed (and, thus, frequency), which is usually considerably higher than the 0-Hz operation point. The converter does not need to take the turbine out from its inertial state since the wind itself can make the turbine start moving. When the WT is producing its nominal power, on the other hand, it will be controlled to its nominal speed that corresponds to its nominal frequency, which is equal to the grid frequency [17]. In this case, the  $M^3C$  would face instability if it was used to drive the WT.

Recently, a new converter topology was presented and it was named modular multilevel shunt converter (MMSHC) [18]–[20]. In [19], the MMSHC was proposed with integrated batteries into each submodule and the high-power WT driven by it was capable to operate in a dispatchable fashion providing benefits to both the power system operator and to the WT owner. Nonetheless, a drawback of this configuration was that the batteries had to be charged/discharged with the full WT power and, thus, a large battery system was required, and the battery-system lifetime was reduced. In order to solve this problem, in [20], a hybrid version of the MMSHC was proposed in which each string was built with part of its submodules with integrated batteries and part of its submodules with integrated capacitors. The submodule capacitors were responsible for transferring most of the power generated by the WT to the grid and the batteries only absorbed/supplied the surplus between the power produced by the WT and the power to be injected into the grid according to a pre-defined setpoint. In other words, the WT was still capable to operate in a dispatchable fashion while optimizing the lifetime of the batteries and the battery system dimensions. In the hybrid MMSHC, presented in [20], the submodule-capacitor voltages were regulated by controlling the number of inserted battery

submodules and the converter was always operating supplying to the grid a power value different from the power generated by the WT.

In this paper, the MMSHC with capacitors only is presented (see Fig. 1) as an interesting alternative to drive modern/future high-power medium-voltage WTs. In this case, the WT driven by it is not capable to operate in a dispatchable fashion and a control technique must be applied to the converter in order to regulate its submodule-capacitor voltages. Thus, one of the contributions of this paper is the proposal of a control technique to regulate the submodule-capacitor voltages of the converter. Obviously, having an integrated energy storage system (as proposed in [19], [20]) allows the WT to perform many different functionalities, even though the commitment with reduced volume, weight and cost is not the objective of the solution. On the other hand, the converter with capacitors only, presented in this paper, has the potential to result in a WT solution with an overall reduced weight, volume and cost, because of its medium-voltage structure and due to the fact that the proposed converter presents a reduced number of submodules, capacitors and inductors, in comparison to other modular multilevel converters, as will be demonstrated through a comparative analysis presented in this work. Thus, another important contribution of this paper is the presentation of this comprehensive comparative analysis between the MMSHC, the MMC and the  $M^3C$ , which proves that the MMSHC can be built with a considerably reduced number of submodules, in comparison to the other two topologies, which means it requires a reduced number of the bulky, heavy and expensive submodule capacitors. Moreover, the comparative analysis demonstrates that the MMSHC presents a reduced inductance requirement, in comparison to the other two topologies, which further contributes to a reduced weight and volume. These are attractive features for a converter used to drive WTs, especially offshore ones that require complex foundations to support the system. Moreover, in opposition to the  $M^3C$ , the MMSHC is capable to operate with the same frequency at its grid-side and load-side terminals, as will be demonstrated in this paper. Similarly to the conventional MMC, the AC submodule-capacitor voltage ripple of the proposed topology is critical at very low frequencies, but it is extremely reduced for increased frequency values. Since WT applications do not require operation at very low frequencies, then both the MMC and the proposed solution should not experience a critical capacitor voltage ripple in these applications. As explained in [19], [20], the MMSHC does not have circulating currents, which is a consequence of its topology and operation, where different submodule strings are never connected, simultaneously, to the same terminal. First, because each phase is composed of two submodule strings that are independent from the submodule strings of the other two phases, i.e., submodule strings from different phases are never connected to the same terminal. Second, because even the two submodule strings of the same phase operate in a complementary fashion, i.e., they are connected to the grid and to the generator terminals in an alternate fashion through the action of the swap switches. The absence of circulating currents can be considered as an advantage in relation to other topologies with a modular multilevel

structure since these currents must be suppressed to limit the conduction losses of the converter. As will be shown in this paper, another advantage of the proposed converter topology is the less complex control/modulation in comparison to the MMC, but especially in comparison with the M<sup>3</sup>C. Finally, simulation and experimental results are presented to explain and validate the operation of the MMSHC with capacitors only, which is another contribution of this paper. The paper is structured as follows: The operation of the proposed topology and its control are introduced in Section II and Section III, respectively. In Section IV, the comparative analysis between the MMC, the M<sup>3</sup>C and the MMSHC is presented. In Section V and Section VI, simulation and experimental results are shown, respectively. Finally, conclusions are presented in Section VII.

## II. PROPOSED CONVERTER TOPOLOGY

As shown in Fig. 1, each phase of the MMSHC is composed of two strings (String X and String Y) of full-bridge (FB) submodules, along with four bidirectional-switch stacks ( $S_{XA}$ ,  $S_{Xa}$ ,  $S_{YA}$  and  $S_{Ya}$  in the phase-A case) that form the swap-switch circuit. The two submodule strings operate in a complementary fashion, meaning that while one is connected to the grid terminal, the other is connected to the generator terminal and, thus, a continuous power flow is established between the generator and the grid. The alternated connection between grid and generator terminals is made through the control of the swap switches (bidirectional-switch stacks) that allow for the connection of the submodule strings to both terminals. In Fig. 2, an illustration of the MMSHC basic operation is shown using the phase A of the converter as an example. In this figure, it is possible to notice that the MMSHC strings behave as controlled voltage sources that can be connected to both grid and load terminals.

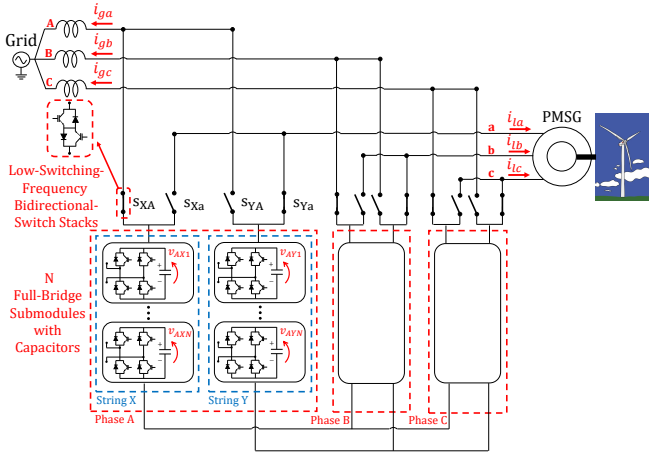


Fig. 1. MMSHC topology.

The MMSHC essentially operates alternating between State 1 and State 2 as described in Fig. 2. In State 1, String X is connected to the grid terminal and it injects into the grid the power  $P_{ga}$ , while String Y is connected to the generator terminal and it absorbs from it the power  $P_{la}$ . In other words, in State 1, the String-X capacitors are discharged and the String-Y capacitors are charged. Since the MMSHC is built with capacitors only, in this paper, then  $P_{ga}$  is controlled to

always be equal to  $P_{la}$  in order to keep the average value of the submodule-capacitor voltages regulated according to the desired reference. In State 2, on the other hand, String Y is connected to the grid terminal and it injects into the grid the power  $P_{ga}$ , while String X is connected to the generator terminal and it absorbs from it the power  $P_{la}$ . It is interesting to notice that while the bidirectional-switch stacks do not operate, the MMSHC essentially is equal to two single-star bridge-cells (SSBC) converters [21]–[23], each connected to a different terminal. In Fig. 3, the SSBC converter topology is shown. This is a well-established solution commonly used in static synchronous compensator (STATCOM) applications. By analyzing Fig. 1, one can notice that the MMSHC is indeed composed of six submodule strings (two for each phase). The operation of the swap switches is done in a way that the Strings X of each phase are simultaneously connected to the same terminal while the Strings Y of each phase are simultaneously connected to the opposite terminal. Thus, there are two different neutral points (see Fig. 1) in the converter: one connecting the Strings X of each phase and the other connecting the Strings Y of each phase. This way, the MMSHC basically operates as two independent SSBC converters that are connected, in a complementary fashion, to the grid and to the turbine terminals.

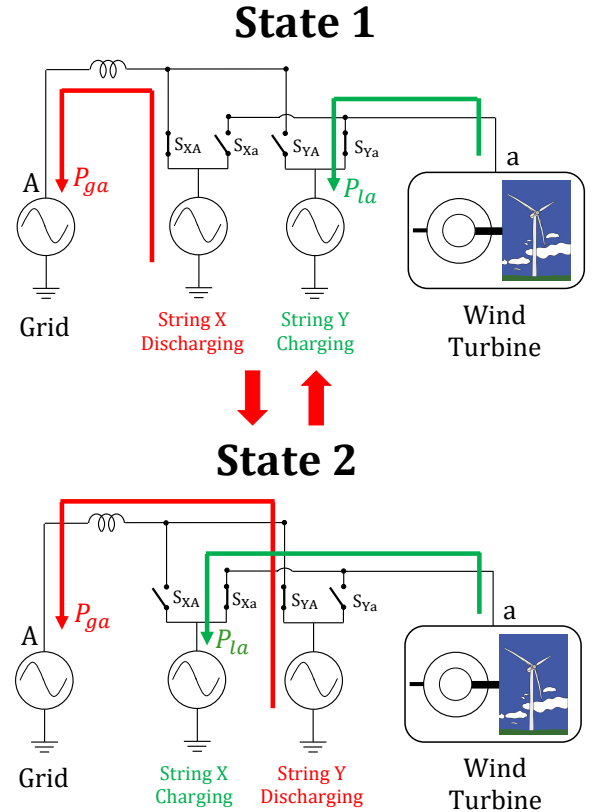


Fig. 2. Basic operation of the MMSHC.

As previously mentioned, the MMSHC swap switches are composed of bidirectional-switch stacks, which are sensitive components of the topology that deserve special attention. In other words, since the MMSHC is proposed for medium-voltage WT applications, then the bidirectional-switch stacks might need to be built with series-connected semiconductor

devices. The voltage across the stacks in blocking mode is equal to the difference between the instantaneous value of the voltage synthesized by String X and the instantaneous value of the voltage synthesized by String Y. Thus, these stacks must be capable to withstand the sum of the peak values of the voltages synthesized by each string, considering that these voltages might present different frequencies. Nonetheless, it is important to emphasize that since the medium-voltage levels considered for high-power WT applications are usually in the range of 3 kV up to 6.6 kV [3], then only a few series-connected semiconductor devices should be required to build the MMSHC bidirectional-switch stacks. Besides, nowadays, there are semiconductor devices available in the industry with voltage ratings of 6.5 kV, and some others with voltage ratings of up to 10 kV under test, which emphasizes even more the necessity of only few series-connected devices to build the MMSHC stacks. There are some products available in the industry that correspond to stacks composed of several series-connected semiconductor devices, and that operate with high reliability due to advanced drivers that ensure static and dynamic voltage sharing among the series-connected devices [8]. These stacks could be adopted to build the MMSHC swap switches. Finally, another important characteristics of the MMSHC swap switches is that they can operate with low switching frequencies as will be demonstrated in this paper. As previously mentioned, the problems of operating series-connected devices in TL converters, for example, are amplified because of the high switching frequencies used in such topology. The low switching frequency of the MMSHC bidirectional-switch stacks makes it easier to operate the series-connected devices in a safe and reliable manner. Even the use of snubber circuits with reduced losses would be possible due to the low switching frequency of the MMSHC stacks. Besides, the low switching frequency of the MMSHC swap switches would lead to low switching losses. The commutation strategy of the swap switches was discussed and explained in [19], in which techniques such as the four-step method, commonly applied to matrix converters [24], [25], were suggested. This topic will not be discussed in this paper.

The classification of the proposed converter solution lies between converters with a purely modular multilevel structure and converters built with stacks of series-connected semiconductor devices operating at high switching frequencies, i.e., the MMSHC is built with a combination of submodule strings (as in any converter with a modular multilevel structure) and of stacks of series-connected semiconductor devices. Because of this combination, the proposed converter is capable to synthesize a high-power-quality multilevel voltage, as any converter with a modular multilevel structure, while presenting a considerably reduced volume and weight because of its overall reduced component count. Its modular multilevel structure also presents the traditional features of being scalable, redundant, and reliable. All these features related to the modular multilevel strings are beneficial in comparison to the converters built with stacks of series-connected devices operating at high frequencies such as the TL converter and the NPC converter. Nonetheless, the bidirectional-switch stacks of the proposed converter solution might reduce its reliability in comparison to the converters with a purely modular multilevel structure. Still, it is important to highlight that the stacks of series-connected semiconductor devices of the MMSHC operate with an extremely low switching frequency, which makes them considerably more reliable and efficient than the stacks of series-connected semiconductor devices operating at high switching frequencies of the TL converter and of the NPC converter. In summary, the advantages of the proposed MMSHC in comparison to the TL converter and to the NPC converter are the improved power quality of the synthesized voltages and, thus reduced filtering requirements, and the improved reliability to operate at increased voltages due to the use of the reliable submodule strings along with series-connected semiconductor devices operating with a considerably lower switching frequency. Nonetheless, the MMSHC presents increased structural and operational complexity in comparison to the TL converter and to the NPC converter. The advantages of the proposed MMSHC in comparison to the MMC and the M<sup>3</sup>C are its reduced operational complexity, its reduced component count, and its possibly reduced capacitance and inductance requirements that potentially leads to reduced cost, volume, and weight. Nonetheless, the MMSHC presents a reduced reliability in comparison to the MMC and the M<sup>3</sup>C since it is not a converter purely based on submodule strings, i.e., it presents the bidirectional-switch stacks built with series-connected semiconductor devices. As previously mentioned, even though these stacks operate with a low switching frequency, they are still less reliable than the highly reliable strings of submodules. The comparative information above presented suggests that the proposed converter solution could represent an interesting trade-off in terms of benefits and drawbacks in relation to the other topologies as summarized in TABLE I. Obviously, as any other engineering solution, the proposed converter presents advantages and disadvantages in comparison to other well-established topologies that are available in the industry, and the best solution to be adopted will depend on the specific application considered.

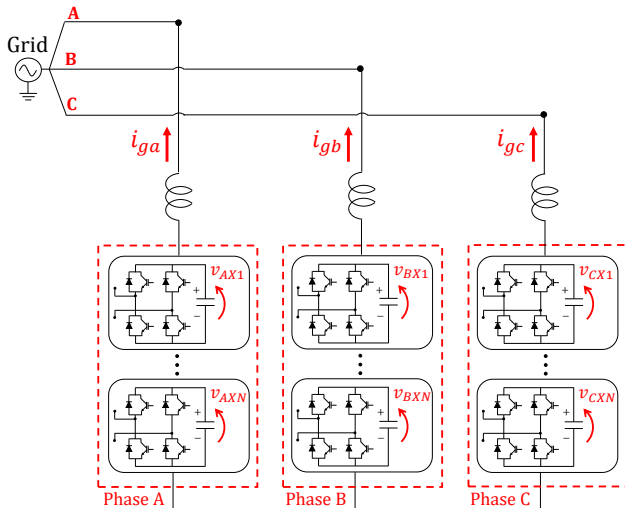


Fig. 3. SSBC converter topology.

TABLE I  
SUMMARY OF FEATURES OF CONVERTER TOPOLOGIES.

Converter Topology	Filtering Requirements	Component Count	Reliability at High Voltages	Structural and Control Complexity
TL Converter	High	Low	Low	Low
NPC Converter	High	Low	Low	Low
MMC	Low	High	High	High
M <sup>3</sup> C	Low	High	High	High
MMSHC	Low	Average	Average	Average

### III. MMSHC CONTROL AND MODULATION

In this section, the MMSHC's grid-side and load-side closed-loop control strategies are presented along with the converter's internal control as shown in Fig. 4. The MMSHC's grid-side control is responsible for regulating the converter's submodule-capacitor voltages, and it generates the reference for the voltages to be synthesized at the grid terminals ( $v_{gabc}^*$ ). As shown in Fig. 4, the MMSHC's grid-side control is composed of three single-phase block diagrams. Each of these single-phase control diagrams is responsible for regulating the submodule-capacitor voltages of Strings X and Y of the corresponding converter phase. The phase-A grid-side control block diagram is shown in Fig. 4 as an example, and it is used to regulate the submodule-capacitor voltages of Strings X and Y of the MMSHC's phase A. The details of this control diagram will be explained later in this section. In this paper, the MMSHC's load-side control is responsible for regulating the speed of the PMSG, and it generates the reference for the voltages to be synthesized at the generator terminals ( $v_{labc}^*$ ). The block diagram presenting the MMSHC load-side control is shown in Fig. 4 and it will also be explained later in this section.

The MMSHC's internal control essentially consists of the bidirectional-switch-stack control logic, of the modulation, and of the sorting algorithm responsible for the submodule-capacitor voltage balancing. The converter's internal control is a single-phase algorithm that is applied to each phase of the converter (see Fig. 4). The MMSHC's phase-A internal control is explained through the flowchart shown in Fig. 5, which is the same control algorithm used for the other two phases. In the simulation and experimental analyses presented in this paper, this control algorithm was implemented through a programming code. The converter's internal control receives as input the voltage references for both grid terminals ( $v_{gk}^*$ ) and load terminals ( $v_{lk}^*$ ), which come from the grid-side and load-side controllers, where  $k$  represents the given converter phase. Since in Fig. 5 the internal control of the MMSHC's phase A is explained, then the references coming from the outer controllers are  $v_{ga}^*$  and  $v_{la}^*$ . The MMSHC's phase-A internal control also receives as input the currents measured at the converter's load and grid terminals ( $i_{la}$  and  $i_{ga}$ , respectively), and the capacitor voltages of all the  $N$  submodules within String X and of all the  $N$  submodules within String Y ( $v_{AX1}, v_{AX2}, \dots, v_{AXN}, v_{AY1}, v_{AY2}, \dots, v_{AYN}$ ). Finally, the MMSHC's internal control receives as input a triangular signal ( $tri$ ), which varies between 0 and 1, and that is used for the bidirectional-switch-stack control logic.

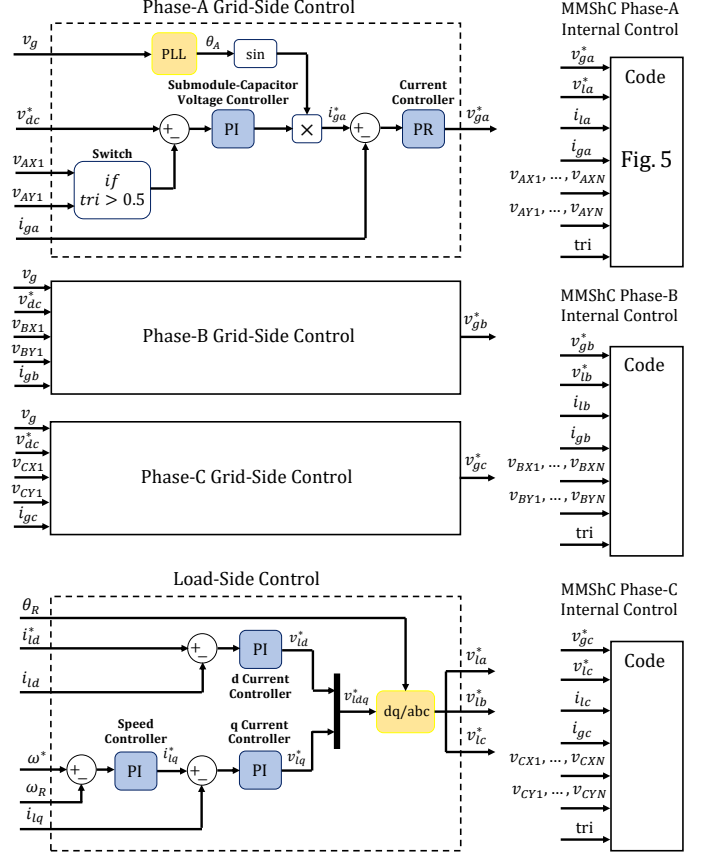


Fig. 4. General diagram of MMSHC's control.

The first step of the MMSHC's internal control is the bidirectional-switch-stack operation logic. An *if* statement is used to check if the variable  $tri$  is greater or less than 0.5. If  $tri > 0.5$ , then String X should be connected to the generator terminal (charging mode) and String Y should be connected to the grid terminal (discharging mode). This operation mode corresponds to State 2 of Fig. 2. In this case, the following gate signals are given to the bidirectional-switch stacks:  $S_{XA} = 0$ ,  $S_{Xa} = 1$ ,  $S_{YA} = 1$  and  $S_{Ya} = 0$ , in which 0 means OFF state and 1 means ON state. Besides, in this operation mode, the voltage to be synthesized across String X becomes equal to the load voltage reference ( $v_{sX}^* = v_{la}^*$ ), the voltage to be synthesized across String Y becomes equal to the grid voltage reference ( $v_{sY}^* = v_{ga}^*$ ), the String-X current becomes equal to the load current ( $i_X = i_{la}$ ), and the String-Y current becomes equal to the grid current ( $i_Y = i_{ga}$ ). On the contrary, if  $tri < 0.5$ , then String X should be connected to the grid terminal (discharging mode) and String Y should be connected to the generator terminal (charging mode).



mode). This operation mode corresponds to State 1 of Fig. 2. In this case, the following gate signals are given to the bidirectional-switch stacks:  $S_{XA} = 1$ ,  $S_{Xa} = 0$ ,  $S_{YA} = 0$  and  $S_{Ya} = 1$ . Besides, in this operation mode, the voltage to be synthesized across String X becomes equal to the grid voltage reference ( $v_{sX}^* = v_{ga}^*$ ), the voltage to be synthesized across String Y becomes equal to the load voltage reference ( $v_{sY}^* = v_{la}^*$ ), the String-X current becomes equal to the grid current ( $i_X = i_{ga}$ ), and the String-Y current becomes equal to the load current ( $i_Y = i_{la}$ ). In the simulation analyses of this paper, two different frequency values are adopted for the triangular signal (*tri*), i.e., 50 Hz and 150 Hz, which means that the bidirectional-switch stacks operate with switching frequencies of either 50 Hz or 150 Hz.

The next stage of the algorithm is the String-X and String-Y control. Considering the String-X control as an example, the first step is the modulation that receives as input the voltage reference  $v_{sX}^*$  and provides as output the instantaneous number of submodules to be inserted (*M*) and the polarity of the submodules to be inserted in order to track the received voltage reference. The modulation method adopted in this paper is the well-established level-shifted-carrier pulse-width modulation (LSC-PWM). The next step after the modulation is the sorting algorithm responsible for the submodule-capacitor-voltage balancing. This algorithm essentially checks the polarity of the submodules to be inserted (polarity of  $v_{sX}^*$ ) and the direction of the current  $i_X$ . Depending on the combination of voltage polarity and current direction, the current can be charging or discharging the capacitors of the inserted submodules. Then, if it is a charging current, the *M* submodules, out of the *N* available submodules, with lower capacitor voltages are selected to be inserted. On the contrary, if it is a discharging current, the *M* submodules with higher capacitor voltages are selected to be inserted. This algorithm guarantees that all the submodule capacitors within the same string remain with similar voltage values. The same procedure is adopted for String Y. The output of the control algorithm implemented in a programming code are the gate signals provided to the bidirectional-switch stacks ( $S_{XA}$ ,  $S_{Xa}$ ,  $S_{YA}$  and  $S_{Ya}$ ), and the gate-signal vectors that are provided to the IGBTs of the *N* submodules within String X ( $\vec{S}_{FB1AX}, \vec{S}_{FB2AX}, \dots, \vec{S}_{FBNAX}$ ) and to the IGBTs of the *N* submodules within String Y ( $\vec{S}_{FB1AY}, \vec{S}_{FB2AY}, \dots, \vec{S}_{FBNAY}$ ). For example, the vector  $\vec{S}_{FB1AX}$  is equal to  $\vec{S}_{FB1AX} = [S_{FB1AX1}, S_{FB1AX2}, S_{FB1AX3}, S_{FB1AX4}]$ , in which these four terms correspond to the gate signals provided to the four IGBTs of the FB submodule number one of the MMSHC phase-A String X. Similarly, the vector  $\vec{S}_{FB1AY}$  is equal to  $\vec{S}_{FB1AY} = [S_{FB1AY1}, S_{FB1AY2}, S_{FB1AY3}, S_{FB1AY4}]$ , in which these four terms correspond to the gate signals provided to the four IGBTs of the FB submodule number one of the MMSHC phase-A String Y. It is important to notice that this is a quite straightforward internal control, with a reduced complexity in comparison to the internal control of the MMC and of the M<sup>3</sup>C. For example, undesired circulating currents are non-existent, which obviously avoids the need of a circulating-current suppression control. The

simplified control and modulation is an important advantage of the proposed MMSHC, especially in comparison to the M<sup>3</sup>C that presents extremely complex control and modulation [6], [12]–[16].

As previously mentioned, the MMSHC's phase-A grid-side-control block diagram is shown in Fig. 4. This control diagram is essentially composed of an inner current-control loop, based on a proportional-resonant (PR) controller, and of an outer control loop, based on a proportional-integral (PI) controller to regulate the submodule-capacitor voltages. As previously explained, the MMSHC operates connecting its submodule strings, alternately, to the grid and to the load terminals according to the signal *tri* as demonstrated in Fig. 5. Thus, the submodule-capacitor voltage control requires a block (Switch) to receive capacitor-voltage measurements from both submodule strings (String X and String Y) in an alternate fashion. If the signal *tri* is greater than 0.5, then String Y is the one connected to the grid terminal and, thus, its submodule capacitors are the ones whose voltages must be regulated. In this case, the voltage controller will receive as an input the error between the measured capacitor voltage of the first submodule of String Y ( $v_{AY1}$ ) and the desired voltage reference  $v_{dc}^*$ . Even though the measured capacitor voltage of the first submodule of String Y was considered in this case, any other capacitor voltage of any submodule within String Y could be used since a sorting algorithm is adopted to maintain all the capacitors within the same submodule string with similar voltage values. On the contrary, if the signal *tri* is less than 0.5, then String X is the one connected to the grid terminal and, thus, its submodule capacitors are the ones whose voltages must be regulated. In this case, the voltage controller will receive as an input the error between the measured capacitor voltage of the first submodule of String X ( $v_{AX1}$ ) and the same desired voltage reference  $v_{dc}^*$ . The output of the submodule-capacitor voltage controller is the amplitude of the current reference ( $i_{ga}^*$ ) that is multiplied by a *sin* function with the angle of the phase-A grid voltage ( $\theta_A$ ). In other words, since the grid-side control is responsible for regulating the submodule-capacitor voltages by charging/discharging these capacitors with active power, then the phase-A grid-current reference ( $i_{ga}^*$ ) must be in phase with the phase-A grid voltage ( $v_{ga}$ ). The inner current controller will generate the phase-A grid-side-control voltage reference ( $v_{ga}^*$ ) that is provided to the MMSHC internal control explained in Fig. 5. It is important to emphasize that, even though the control technique shown in Fig. 4 was adopted in this paper, any other well-established control method applied to the SSBC converter to regulate its submodule-capacitors voltages [21]–[23] could potentially be used in the MMSHC.

Finally, the MMSHC's load-side control, shown in Fig. 4, is based on a field-oriented control (FOC) technique. In this control strategy, two inner control loops are used to regulate the generator current in a *dq* rotating reference frame. The *q*-axis current component is used to control the machine speed. The *q*-axis current controller is connected in cascade with an outer speed controller used to regulate the generator speed ( $\omega_R$ ) according to a given reference ( $\omega^*$ ). The FOC generates a voltage reference  $v_{lab}^*$  to be synthesized by the

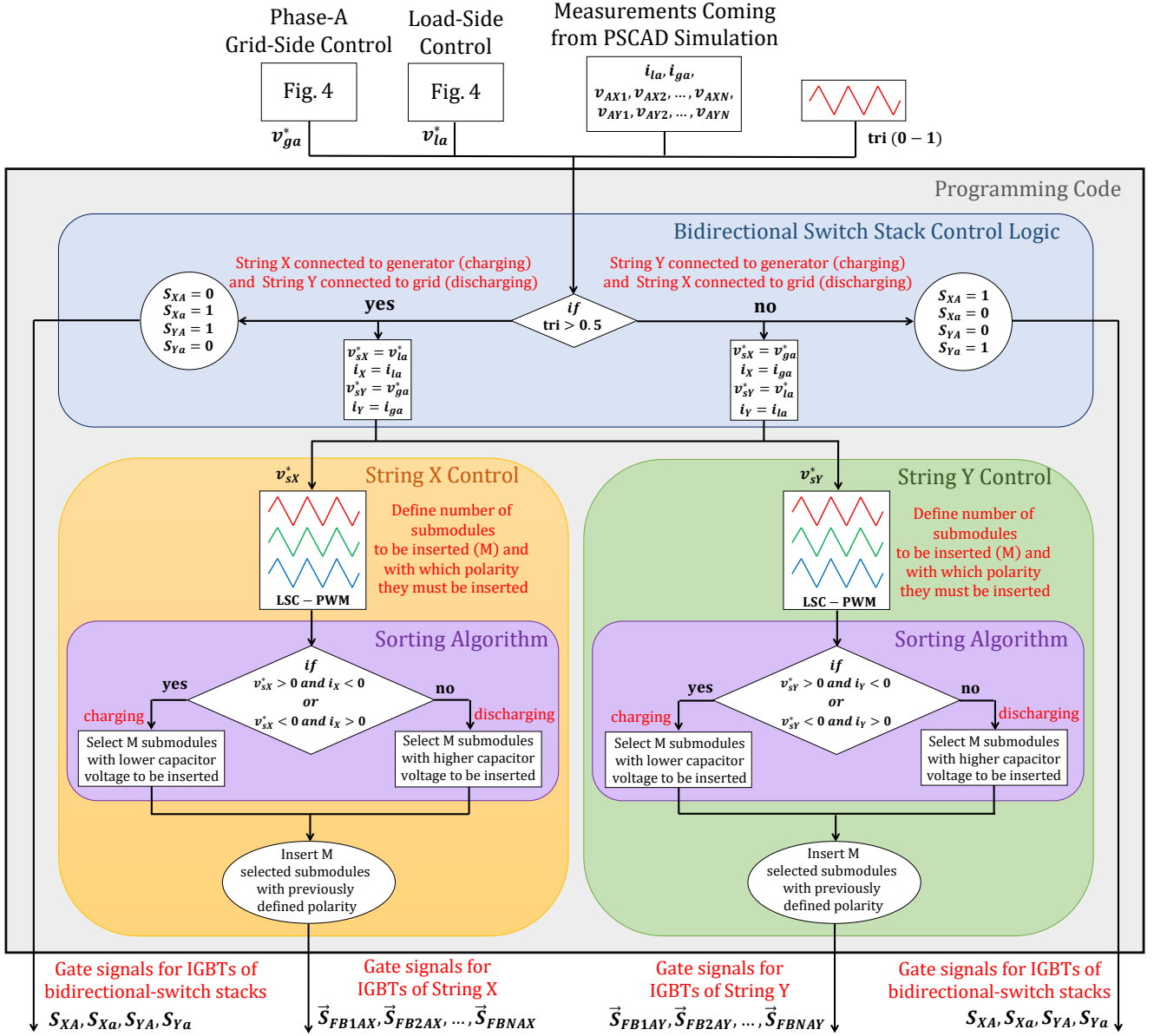


Fig. 5. MMSHC's phase-A internal control implemented through a programming code.

MMSHC at the generator terminals. In the phase-A internal control case,  $v_{la}^*$  is received as input as shown in both Fig. 4 and Fig. 5.

#### IV. COMPARATIVE ANALYSIS

In this section, a comparative analysis among the MMC, the M<sup>3</sup>C and the MMSHC in terms of component count and power ratings is presented. To carry out a fair comparative analysis, some assumptions were considered. First, it was considered that the three converter topologies operated synthesizing the same voltage at both their terminals with phase-to-neutral peak value equal to  $V_{peak}$ . Another assumption was that the three converters operated supplying power to the same load, resulting in an equal load current with rms value equal to  $I_{RMS}$ . Finally, it was considered that the three converters operated with an unit power factor at both their load-side and grid-side terminals in such a way that the current injected into

the grid by the converter presented same rms value as the load current ( $I_g = I_l = I_{RMS}$ ). To carry out the comparative analysis in terms of submodule and capacitor count, a fixed IGBT rated voltage equal to  $V_{IGBT}$  was considered for the three converter topologies.

##### A. MMC

The topology of the MMC used for this comparative analysis is shown in Fig. 6. In order for the MMC to be capable to synthesize a voltage with amplitude equal to  $V_{peak}$  at its AC terminals, then its DC-link voltage should ideally be designed as [8]:

$$V_{DC} \geq 2V_{peak} \quad (1)$$

As a natural consequence of the MMC topology and operation, the converter's DC-link voltage is divided among the  $N$  capacitors within one submodule string (one arm of the converter).



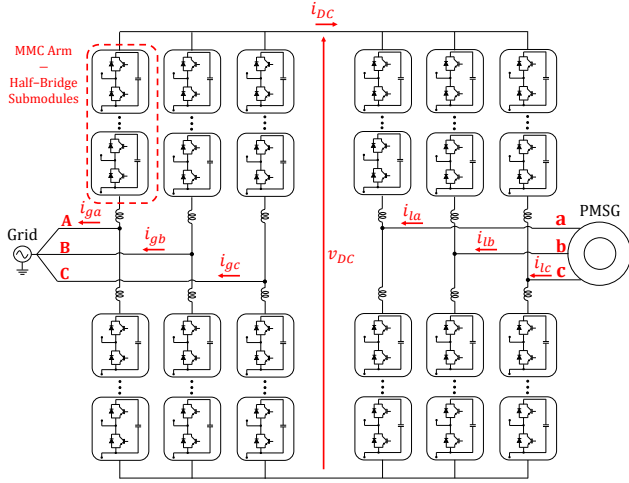


Fig. 6. MMC topology.

Since a sorting algorithm responsible for the submodule-capacitor voltage balancing is always used for the proper operation of the converter, then it is a fair assumption to consider that the nominal operational voltage of each submodule capacitor within one arm ( $V_{cap}$ ) is equal to  $V_{cap} = \frac{V_{DC}}{N}$ . Ideally speaking, the converter's submodules, and their IGBTs, must be able to tolerate at least the capacitor's nominal operational voltage, i.e.:

$$V_{sub} \geq V_{cap} = \frac{V_{DC}}{N} \quad (2)$$

In which  $V_{sub}$  is the maximum voltage that the submodule's IGBTs are capable to withstand. The current that flows through each MMC arm is equal to:

$$I_{arm} = \frac{I_{RMS}}{2} + \frac{I_{DC}}{3} + I_{circ} \quad (3)$$

In which,  $I_{DC}$  is the MMC DC-terminal current and  $I_{circ}$  represents the AC circulating current components. Considering the approximation that the MMC AC-side power is equal to its DC-side power, the following is obtained:

$$V_{DC}I_{DC} = \sqrt{3}\left(\frac{\sqrt{3}V_{peak}}{\sqrt{2}}\right)I_{RMS} \quad (4)$$

Through (4), the MMC DC current can be described as follows:

$$I_{DC} = \frac{3}{\sqrt{2}} \frac{V_{peak}I_{RMS}}{V_{DC}} \quad (5)$$

Based on (1), the ideal case where  $V_{DC} = 2V_{peak}$  is considered and, thus, (5) can be rewritten as:

$$I_{DC} = 1.06I_{RMS} \quad (6)$$

By substituting (6) into (3) and by disregarding the AC circulating current components (considering they are properly compensated), the following is obtained:

$$I_{arm} = 0.85I_{RMS} \quad (7)$$

The MMC is built with half-bridge (HB) submodules that are composed of two IGBTs and of one capacitor. Each IGBT must be capable to withstand the voltage  $V_{sub}$  (defined in (2))

and must be capable to conduct  $I_{arm}$  (defined in (7)). Considering the ideal case where  $V_{sub} = V_{cap} = \frac{V_{DC}}{N} = \frac{2V_{peak}}{N}$  (which means to design the IGBT's rated voltage equal to the submodule-capacitor nominal voltage), then the power ratings of the MMC's semiconductor devices can be calculated as follows:

$$P_{IGBT} = V_{sub}I_{arm} = 1.7 \frac{V_{peak}I_{RMS}}{N} \quad (8)$$

Once again, each MMC's HB submodule has two IGBTs. Each MMC arm is composed of  $N$  HB submodules, and the entire back-to-back MMC is composed of twelve arms. Thus, the total number of IGBTs in the MMC is equal to  $N_{IGBT} = 12 \times N \times 2 = 24N$ . Finally, the total semiconductor-device power ratings of the MMC, as a function of  $V_{peak}$  and  $I_{RMS}$ , is equal to:

$$P_{SD} = P_{IGBT}N_{IGBT} = 40.8V_{peak}I_{RMS} \quad (9)$$

Now, fixing the IGBT's rated voltage with a value equal to  $V_{IGBT}$ , and noticing that the total voltage across the  $N$  submodule capacitors within one MMC arm is equal to  $V_{DC} = 2V_{peak}$  (sum voltage of the  $N$  capacitors), then the number of submodules composing each MMC arm can be calculated as:

$$N = \frac{V_{DC}}{V_{IGBT}} = \frac{2V_{peak}}{V_{IGBT}} \quad (10)$$

Once again, each MMC HB submodule has one capacitor. Each MMC arm is composed of  $\frac{2V_{peak}}{V_{IGBT}}$  HB submodules, and the entire back-to-back MMC is composed of twelve arms. Thus, the total number of submodules and of capacitors in the MMC is equal to  $N_{sub} = N_{cap} = 12 \times \frac{2V_{peak}}{V_{IGBT}} \times 1 = \frac{24V_{peak}}{V_{IGBT}}$ . The back-to-back MMC also requires twelve arm inductors as shown in Fig. 6.

### B. $M^3C$

The topology of the  $M^3C$  considered for this comparative analysis is shown in Fig. 7 below.

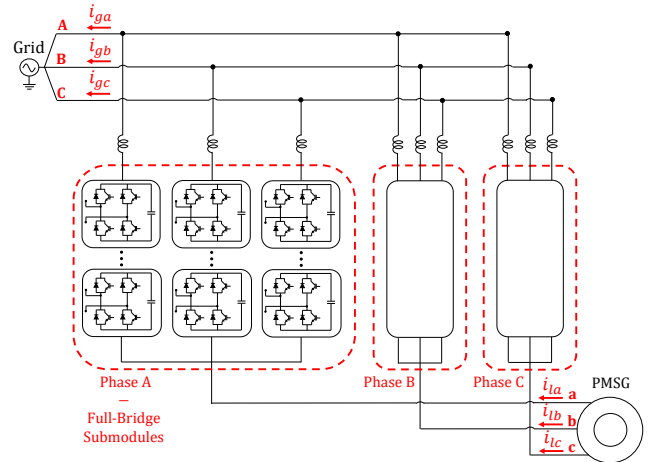


Fig. 7.  $M^3C$  topology.

In order for the  $M^3C$  to be capable to synthesize a voltage with amplitude equal to  $V_{peak}$  at its AC terminals, then its string voltage should ideally be designed as [12]:

$$V_{string} \geq V_g + V_l + V_{com} \quad (11)$$

In which  $V_g$  and  $V_l$  are the peak values of the voltages to be synthesized by the M<sup>3</sup>C at its grid-side and load-side terminals, respectively, and  $V_{com}$  is the common-mode voltage necessary for the proper operation of the converter in certain situations. In this analysis,  $V_g = V_l = V_{peak}$  is considered. Disregarding the common-mode component, then the M<sup>3</sup>C string voltage should ideally be designed as:

$$V_{string} \geq V_g + V_l = 2V_{peak} \quad (12)$$

The M<sup>3</sup>C string voltage is naturally divided among the  $N$  submodule capacitors within the string. Considering that a sorting algorithm is always adopted to maintain all the submodule capacitors within the same string with similar voltage values, then it is a fair assumption to consider that the nominal operational voltage of each submodule capacitor within one string ( $V_{cap}$ ) is equal to  $V_{cap} = \frac{V_{string}}{N}$ . Ideally speaking, the converter's submodules, and their IGBTs, must be able to tolerate at least the capacitor's nominal operational voltage, i.e.:

$$V_{sub} \geq V_{cap} = \frac{V_{string}}{N} \quad (13)$$

In which  $V_{sub}$  is the maximum voltage that the submodule's IGBTs are capable to withstand. The same ideal assumption considered for the MMC is also adopted for the M<sup>3</sup>C, which in the M<sup>3</sup>C case means that  $V_{string} = 2V_{peak}$ , and  $V_{sub} = V_{cap} = \frac{V_{string}}{N} = \frac{2V_{peak}}{N}$ . The current that flows through each M<sup>3</sup>C string is equal to:

$$I_{string} = \frac{I_g}{3} + \frac{I_l}{3} + I_{circ} \quad (14)$$

$I_{circ}$  are the circulating-current components that are essential for the proper and stable operation of the M<sup>3</sup>C. Nonetheless, these components will be neglected in this comparative analysis. Thus, considering that  $I_g = I_l = I_{RMS}$ , then (14) can be rewritten as:

$$I_{string} = \frac{I_{RMS}}{3} + \frac{I_{RMS}}{3} = 0.67I_{RMS} \quad (15)$$

The M<sup>3</sup>C is built with FB submodules that are composed of four IGBTs and of one capacitor. Each IGBT must be capable to withstand the voltage  $V_{sub}$  (defined in (13)) and must be capable to conduct  $I_{string}$  (defined in (15)). Once again, considering the ideal case where  $V_{sub} = V_{cap} = \frac{V_{string}}{N} = \frac{2V_{peak}}{N}$ , then the ideal power ratings of the M<sup>3</sup>C semiconductor devices can be calculated as follows:

$$P_{IGBT} = V_{sub}I_{string} = 1.34 \frac{V_{peak}I_{RMS}}{N} \quad (16)$$

Once again, each M<sup>3</sup>C's FB submodule has four IGBTs. Each M<sup>3</sup>C string is composed of  $N$  FB submodules, and the entire M<sup>3</sup>C is composed of nine strings. Thus, the total number of IGBTs in the M<sup>3</sup>C is equal to  $N_{IGBT} = 9 \times N \times 4 = 36N$ . Finally, the total semiconductor-device power ratings of the M<sup>3</sup>C, as a function of  $V_{peak}$  and  $I_{RMS}$ , is equal to:

$$P_{SD} = P_{IGBT}N_{IGBT} = 48.24V_{peak}I_{RMS} \quad (17)$$

Now, fixing the IGBT's rated voltage with a value equal to  $V_{IGBT}$ , and noticing that the total voltage across the  $N$  submodule capacitors within one M<sup>3</sup>C string is equal to  $V_{string} = 2V_{peak}$  (sum voltage of the  $N$  capacitors), then the

number of submodules composing each M<sup>3</sup>C string can be calculated as:

$$N = \frac{V_{string}}{V_{IGBT}} = \frac{2V_{peak}}{V_{IGBT}} \quad (18)$$

Once again, each M<sup>3</sup>C FB submodule has one capacitor. Each M<sup>3</sup>C string is composed of  $\frac{2V_{peak}}{V_{IGBT}}$  FB submodules, and the entire M<sup>3</sup>C is composed of nine strings. Thus, the total number of submodules and of capacitors in the M<sup>3</sup>C is equal to  $N_{sub} = N_{cap} = 9 \times \frac{2V_{peak}}{V_{IGBT}} \times 1 = \frac{18V_{peak}}{V_{IGBT}}$ . The M<sup>3</sup>C also requires nine string inductors as shown in Fig. 7.

### C. MMSHC

In order for the MMSHC to be capable to synthesize a voltage with amplitude equal to  $V_{peak}$  at its AC terminals, then its string voltage should ideally be designed as:

$$V_{string} \geq V_g + V_l = V_{peak} \quad (19)$$

In which  $V_g$  and  $V_l$  are the peak values of the voltages to be synthesized by the MMSHC at its grid-side and load-side terminals, respectively. The MMSHC string voltage is naturally divided among the  $N$  submodule capacitors within the string. Considering that a sorting algorithm is always adopted to maintain all the submodule capacitors within the same string with similar voltage values, then it is a fair assumption to consider that the nominal operational voltage of each submodule capacitor within one string ( $V_{cap}$ ) is equal to  $V_{cap} = \frac{V_{string}}{N}$ . Ideally speaking, the converter's submodules, and their IGBTs, must be able to tolerate at least the capacitor's nominal operational voltage, i.e.:

$$V_{sub} \geq V_{cap} = \frac{V_{string}}{N} \quad (20)$$

In which  $V_{sub}$  is the maximum voltage that the submodule's IGBTs are capable to withstand. The same ideal assumption considered for the MMC and for the M<sup>3</sup>C is also adopted for the MMSHC, which in the MMSHC case means that  $V_{string} = V_{peak}$ , and  $V_{sub} = V_{cap} = \frac{V_{string}}{N} = \frac{V_{peak}}{N}$ .

The MMSHC's bidirectional-switch stacks must also be considered in the analysis. Each bidirectional-switch stack must be capable to block a voltage equal to the sum of the peak values of the voltages synthesized by the two complementary submodule strings at the grid and at the load terminals, i.e., the voltage ratings of the MMSHC's bidirectional-switch stacks must be designed as follows:

$$V_{BS} \geq V_g + V_l = 2V_{peak} \quad (21)$$

In which  $V_{BS}$  is the maximum voltage that the bidirectional-switch stack can withstand. The expression shown in (21) is based on the assumption considered in this analysis where  $V_g = V_l = V_{peak}$ . The current that flows through each MMSHC string and through each MMSHC bidirectional-switch stack is equal to:

$$I_{string} = I_{BS} = I_g = I_l = I_{RMS} \quad (22)$$

The MMSHC is built with FB submodules that are composed of four IGBTs and of one capacitor. Each IGBT must be capable to withstand the voltage  $V_{sub}$  (defined in (20)) and must be

capable to conduct  $I_{string}$  (defined in (22)). Once again, considering the ideal case where  $V_{sub} = V_{cap} = \frac{V_{string}}{N} = \frac{V_{peak}}{N}$ , then the ideal power ratings of the semiconductor devices of the MMShC's FB submodules can be calculated as follows:

$$P_{IGBT_{FB}} = V_{sub} I_{string} = \frac{V_{peak} I_{RMS}}{N} \quad (23)$$

Each bidirectional-switch stack is composed of two IGBT stacks. Because of the natural operation of a bidirectional switch, each IGBT stack must be capable to withstand the full bidirectional-switch-stack voltage ( $V_{BS} = 2V_{peak}$  in the ideal case) and must be capable to conduct the string current  $I_{BS} = I_{string} = I_{RMS}$ . Then, the ideal power ratings of each IGBT stack of the MMShC bidirectional-switch stacks can be calculated as follows:

$$P_{IGBT_{BS}} = V_{BS} I_{BS} = 2V_{peak} I_{RMS} \quad (24)$$

Each MMShC FB submodule has four IGBTs. Each MMShC string is composed of  $N$  FB submodules, and the entire MMShC is composed of six strings. Thus, the total number of IGBTs in the MMShC FB submodule strings is equal to  $N_{IGBT_{FB}} = 6 \times N \times 4 = 24N$ . Moreover, each MMShC bidirectional-switch stack has two IGBT stacks. The entire MMShC is composed of twelve bidirectional-switch stacks. Thus, the total number of IGBT stacks in the MMShC bidirectional-switch stacks is equal to  $N_{IGBT_{BS}} = 12 \times 2 = 24$ . Finally, the total semiconductor-device power ratings of the MMShC, as a function of  $V_{peak}$  and  $I_{RMS}$ , is equal to:

$$P_{SD} = P_{IGBT_{FB}} N_{IGBT_{FB}} + P_{IGBT_{BS}} N_{IGBT_{BS}} \quad (25)$$

$$= 24V_{peak} I_{RMS} + 48V_{peak} I_{RMS} = 72V_{peak} I_{RMS}$$

Now, fixing the IGBT rated voltage with a value equal to  $V_{IGBT}$ , and noticing that the total voltage across the  $N$  submodule capacitors within one MMShC string is equal to  $V_{string} = V_{peak}$  (sum voltage of the  $N$  capacitors), then the number of submodules composing each MMShC string can be calculated as:

$$N = \frac{V_{string}}{V_{IGBT}} = \frac{V_{peak}}{V_{IGBT}} \quad (26)$$

Once again, each MMShC FB submodule has one capacitor. Each MMShC string is composed of  $\frac{V_{peak}}{V_{IGBT}}$  FB submodules, and the entire MMShC is composed of six strings. Thus, the total number of submodules and of capacitors in the MMShC is equal to  $N_{sub} = N_{cap} = 6 \times \frac{V_{peak}}{V_{IGBT}} \times 1 = \frac{6V_{peak}}{V_{IGBT}}$ . Besides, The MMShC only requires three inductors as shown in Fig. 1.

#### D. Summary

In this subsection, a summary of the results obtained through the comparative analysis is presented. In TABLE II, the semiconductor-device power requirements of each topology are presented. In TABLE III, a summary of the submodule and capacitor count of each topology is presented.

MMC	M <sup>3</sup> C	MMShC
$40.8V_{peak} I_{RMS}$	$48.24V_{peak} I_{RMS}$	$72V_{peak} I_{RMS}$

TABLE III  
SUBMODULE AND CAPACITOR COUNT.

MMC	M <sup>3</sup> C	MMShC
$\frac{24V_{peak}}{V_{IGBT}}$	$\frac{18V_{peak}}{V_{IGBT}}$	$\frac{6V_{peak}}{V_{IGBT}}$

Even though the proposed MMShC presents a reduced number of submodules in comparison to the MMC and the M<sup>3</sup>C, it has the highest semiconductor-device power requirements due to the presence of the bidirectional-switch stacks. The MMShC presents an increase of 76.4% in the semiconductor-device requirements in relation to the MMC and an increase of 49.3% in relation to the M<sup>3</sup>C. Thus, the MMShC will require a higher expenditure with semiconductor devices. The MMC is the topology with the lowest semiconductor-device requirements. However, as shown in TABLE III, the proposed MMShC presents the lowest submodule and capacitor count. The MMC requires four times more submodule and capacitors (an increase of 400%) than the MMShC, and the M<sup>3</sup>C requires three times more submodule and capacitors (an increase of 300%) than the MMShC. These capacitors can be quite bulky, heavy and expensive [8]. Thus, the expressively reduced submodule and capacitor requirements of the new MMShC is an important advantage over the other two topologies, which should result in an overall reduced size, volume and weight. The basic concept for the comparative analysis presented in this section is illustrated in Fig. 8.

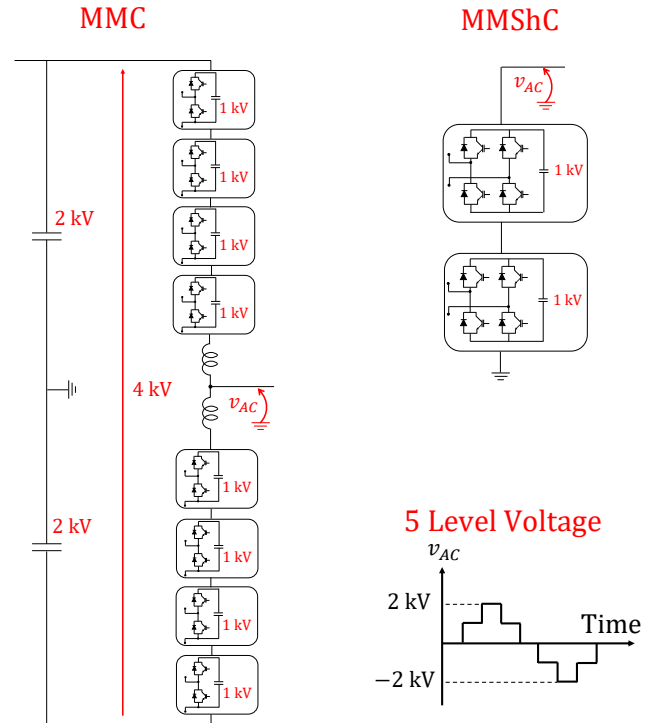


Fig. 8. Illustrative representation of comparative analysis.

In other words, let us consider a situation where a 5-level voltage with peak value equal to 2 kV (see the lower-right sub figure of Fig. 8) is to be synthesized by the MMC and by the MMShC using 1-kV IGBTs. In an ideal case, the nominal capacitor voltage of each submodule could be equal to 1 kV. As shown in the left-hand side of Fig. 8, the MMC

leg (composed of the upper and of the lower arms) would have to be built with eight 1-kV HB submodules to be able to synthesize the desired voltage. The MMSHC string could be built with only two 1-kV FB submodules (see the upper-right sub figure of Fig. 8) to be capable to synthesize the same desired voltage. Since the back-to-back MMC is composed of six legs and the MMSHC is composed of six strings, then the MMC would have to be built with four times more submodules than the MMSHC to be capable to synthesize the same voltage. This is the conclusion reached in the comparative analysis, which is summarized in TABLE III. Even though the capacitor is the bulkiest and heaviest element of a submodule, other elements such as the heat sink, the mechanical by-pass switch, and the submodule structure itself also play an important role in the total volume and weight of a submodule. Thus, having a reduced number of submodules should contribute for an overall reduced volume and weight of the converter solution. Besides, the relation between a capacitor capacitance and its volume and weight is not completely linear, i.e., one 1-kV 10-mF capacitor should be lighter and more compact than two 1-kV 5-mF capacitors. Finally, there should be a considerable space between each submodule for insulation purposes, thus, the total space occupied by two submodules with 1-kV 5-mF capacitors is certainly bigger than the space occupied by one single submodule with a 1-kV 10-mF capacitor. This means that, despite the total converter capacitance, and how this capacitance is distributed among the submodule strings, having a reduced number of submodules and of capacitors should contribute for an overall reduced volume and weight. Nonetheless, the size of the submodule capacitors of each converter should obviously be considered in the comparative analysis. The size (capacitance) of the submodule capacitors should be designed with a value high enough to keep the voltage ripple limited within an acceptable range. The MMC's submodule-capacitor voltage ripple can be mathematically described as follows: In order to synthesize an AC voltage with frequency  $\omega$ , the MMC arms must operate inserting and by-passing submodules with the following pattern:

$$S_{MMC}(t) = 0.5\sin(\omega t) + 0.5 \quad (27)$$

$S_{MMC}(t)$  is a sinusoidal signal that varies between 0 and 1, where 0 means that all the submodules in the arm are by-passed, whereas 1 means that all the submodules in the arm are inserted. The instantaneous MMC arm current is described as follows, disregarding circulating currents:

$$i_{arm}(t) = \frac{i_{AC}(t)}{2} + \frac{i_{DC}(t)}{3} \quad (28)$$

Let us suppose that the MMC operates synthesizing a given AC voltage that results in the following AC current:

$$i_{AC}(t) = I_{peak}\sin(\omega t + \theta) \quad (29)$$

Supposing an operation with unit power factor and considering the approximation that the MMC AC-side power is equal to its DC-side power, then the following equation is obtained:

$$\sqrt{3}\left(\frac{\sqrt{3}}{\sqrt{2}}V_{peak}\right)\frac{I_{peak}}{\sqrt{2}} = V_{DC}I_{DC} \quad (30)$$

Rearranging (30), the following expression is obtained for the DC current:

$$i_{DC}(t) = I_{DC} = \frac{3V_{peak}I_{peak}}{2V_{DC}} \quad (31)$$

By substituting (29) and (31) into (28), the following expression is obtained:

$$i_{arm}(t) = \frac{I_{peak}}{2}\sin(\omega t + \theta) + \frac{V_{peak}I_{peak}}{2V_{DC}} \quad (32)$$

The current that flows through the MMC submodule capacitors causing the AC voltage ripple can be calculated as follows:

$$i_{capMMC}(t) = S_{MMC}(t)i_{arm}(t) \quad (33)$$

In order to synthesize an AC voltage with frequency  $\omega$ , the MMSHC strings must operate inserting and by-passing submodules with the following pattern:

$$S_{MMSHC}(t) = \sin(\omega t) \quad (34)$$

$S_{MMSHC}(t)$  is a sinusoidal signal that varies between  $-1$  and  $1$ , where  $-1$  means that all the submodules in the string are inserted with negative polarity, whereas  $1$  means that all the submodules in the string are inserted with positive polarity. Considering the exact same AC current as in the MMC case, then the instantaneous MMSHC string current is described as follows:

$$i_{string}(t) = i_{AC}(t) = I_{peak}\sin(\omega t + \theta) \quad (35)$$

The current that will flow through the MMSHC submodule capacitors causing the AC voltage ripple can be calculated as follows:

$$i_{capMMSHC}(t) = S_{MMSHC}(t)i_{string}(t) \quad (36)$$

Considering  $I_{peak} = 1$  kA and considering  $V_{DC} = 2V_{peak}$  (see (1)), then the MMC's arm current and the MMSHC's string current can be described as follows:

$$i_{arm}(t) = 0.5\sin(\omega t + \theta) + 0.25 \text{ kA} \quad (37)$$

And

$$i_{string}(t) = \sin(\omega t + \theta) \text{ kA} \quad (38)$$

By substituting (27) and (37) into (33) the following capacitor current is obtained:

$$i_{capMMC}(t) = [0.5\sin(\omega t) + 0.5] \times [0.5\sin(\omega t + \theta) + 0.25] \text{ kA} \quad (39)$$

By substituting (34) and (38) into (36) the following capacitor current is obtained:

$$i_{capMMSHC}(t) = \sin(\omega t) \times \sin(\omega t + \theta) \text{ kA} \quad (40)$$

Considering the following trigonometric identity:

$$\sin^2(\omega t) = \frac{1 - \cos(2\omega t)}{2} \quad (41)$$

Then (39) can be rewritten as follows if  $\theta = 0$ :

$$i_{capMMC}(t) = -0.125\cos(2\omega t) + 0.375\sin(\omega t) + 0.25 \text{ kA} \quad (42)$$

Similarly, considering (41) and  $\theta = 0$ , then (40) can be rewritten as follows:

$$i_{capMMSHC}(t) = -0.5\cos(2\omega t) + 0.5 \text{ kA} \quad (43)$$

By analyzing the MMC's and the MMSHC's capacitor currents described in (42) and (43), respectively, it is clear that the capacitor voltage ripple will be higher for the MMC case than for the MMSHC case. In other words, the capacitor reactance is inversely proportional to the frequency of the current flowing through it ( $X_C = \frac{1}{\omega C}$ ). Let us consider a situation where  $\omega = 314.16 \text{ rad/s}$  (corresponding to 50 Hz), and where  $C = \frac{1}{314.16}$  in such a way that the capacitor reactance for the  $\omega$  component is equal to  $1 \Omega$  and the capacitor reactance for the  $2\omega$  component is equal to  $0.5 \Omega$ . In this case, the voltage drop (voltage ripple) for the MMC's  $\omega$  component will be equal to  $V_{ripple} = 0.375 \times X_C = 0.375 \times 1 = 0.375 \text{ kV}$ , while the voltage drop (voltage ripple) for the MMSHC's  $2\omega$  component will be equal to  $V_{2\omega ripple} = 0.5 \times X_C = 0.5 \times 0.5 = 0.25 \text{ kV}$ . The MMC's  $\omega$  ripple is considerably bigger than the MMSHC's  $2\omega$  ripple. In the MMC case, there is still a second ripple component caused by the  $2\omega$  current. This voltage ripple will have an amplitude equal to  $V_{2\omega ripple} = 0.125 \times X_C = 0.125 \times 0.5 = 0.0625 \text{ kV}$ . The  $2\omega$  ripple component can add up to the  $\omega$  one, resulting in an increased overall voltage ripple.

To validate the previously explained analysis, a simple simulation was performed as shown in Fig. 9. In this simulation, the MMC's and the MMSHC's capacitor currents described by (42) and (43) were separately applied to a current source, and these currents were used to charge a 1-mF capacitor. A high-pass filter was used to eliminate the DC components of the two currents in such a way that only the AC ripple could be observed in the measured capacitor voltages.

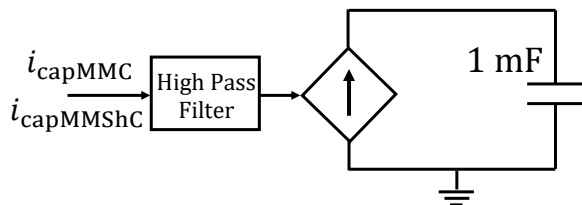


Fig. 9. Simulation to observe and compare the MMC's and the MMSHC's submodule-capacitor voltage ripple.

In Fig. 10(a), the MMC's and the MMSHC's capacitor currents described by (42) and (43) are shown (considering  $\theta = 0$ ). In Fig. 10(b), the corresponding MMC's and MMSHC's submodule-capacitor voltage ripple is shown. As expected from the mathematical analysis previously presented, the MMC's submodule-capacitor voltage ripple is in fact bigger than the MMSHC's one. It is well-known that the MMC's submodule-capacitor voltage ripple can vary depending on its power factor [26]. To observe this variation, different values for the angle  $\theta$  were considered, and the corresponding results are shown in Fig. 11(a) and (b).

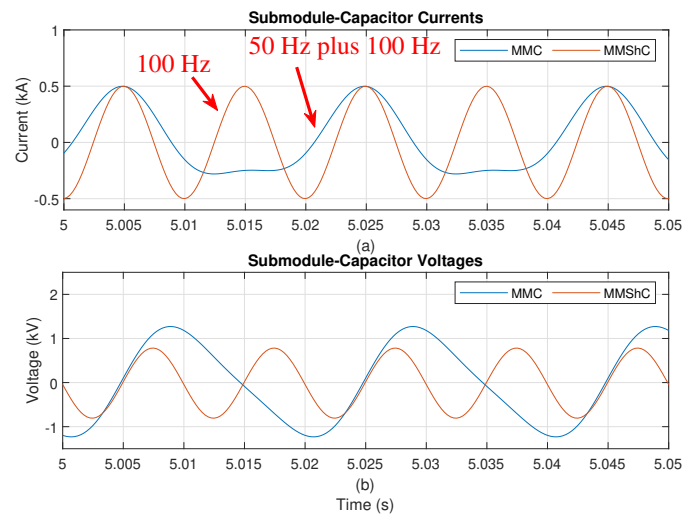


Fig. 10. Simulation results to compare MMC and MMSHC submodule-capacitor voltage ripple. (a) MMC and MMSHC capacitor currents, and (b) MMC and MMSHC submodule-capacitor voltage ripple.

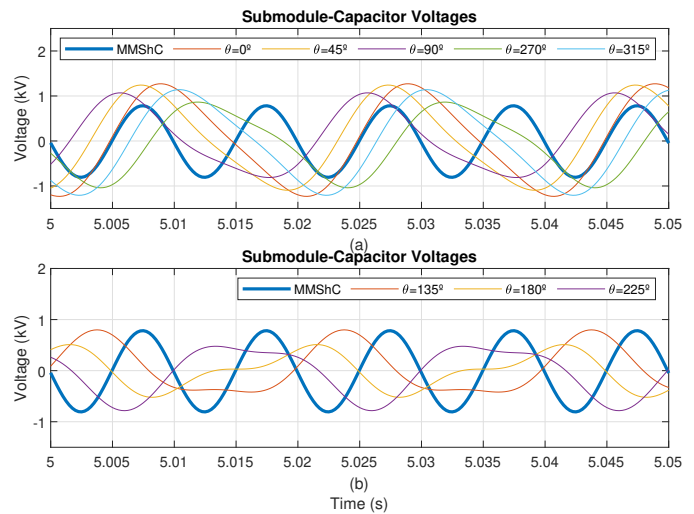


Fig. 11. Simulation results to compare MMC and MMSHC submodule-capacitor voltage ripple. (a) Cases where MMC's submodule-capacitor voltage ripple is higher than MMSHC's one, and (b) cases where MMC's submodule-capacitor voltage ripple is lower than MMSHC's one.

In Fig. 11(a), the cases where the MMC's submodule-capacitor voltage ripple is greater than the MMSHC's one are shown while, in Fig. 11(b), the cases where the MMC's submodule-capacitor voltage ripple is less than the MMSHC's one are shown. As shown in Fig. 11(a), the MMC's capacitor voltage ripple is considerably bigger than the MMSHC's capacitor voltage ripple in many cases. Thus, it can be concluded that the total capacitance in one MMC arm needs to be bigger than the total capacitance in one MMSHC string so that the same AC voltage ripple is obtained in the worst-case scenario. According to the results shown in Fig. 11(a), the MMC's arm capacitance should be approximately 1.63 times bigger than the MMSHC's string capacitance. Since the back-to-back MMC is composed of twelve arms and the MMSHC is composed of six strings, then the total MMC's capacitance should be approximately 3.25 times bigger than the MMSHC's capacitance in order to maintain the AC submodule-capacitor voltage ripple of the two topologies similar in the worst-case scenario.

The previously explained analysis corresponds to what is referred to as the AC ripple of the MMSHC. However, the MMSHC's submodule-capacitor voltage also presents what is referred to as the swapping ripple, which will be explained in detail later in this paper. The swapping ripple is caused by the DC component of the capacitor current, which charges and discharges the submodule capacitors depending if the corresponding string is connected to the grid (discharging) or connected to the wind turbine (charging). The submodule-capacitor swapping ripple will be higher or lower depending on the amount of power handled by the converter. The submodule-capacitor swapping ripple will be higher or lower also depending on the total capacitor energy in the MMSHC's strings. The capacitor energy increases proportionally to the capacitance and with the square of the capacitor voltage ( $E_c = \frac{1}{2}CV^2$ ). Thus, adopting increased voltage levels will contribute to a reduced swapping ripple since the capacitor voltages will suffer a smaller variation before a swapping action occurs connecting the submodule string to the opposite terminal. In any case, the amplitude of the swapping ripple can be reduced by increasing the switching frequency of the MMSHC's bidirectional-switch stacks (swap switches), i.e., the faster the submodule strings are swapped between the charging and discharging terminals, the smaller will be the capacitor voltage variation caused by the DC current component. In summary, the swapping ripple might lead to the requirements of increased capacitance values for the MMSHC if it is desired to keep the switching frequency of the swap switches low, i.e., the trade-off between having a reduced swapping ripple (and thus reduced capacitance requirements), and having improved reliability (due to the low switching frequency of the swap switches) will have to be assessed in the design stage of the converter solution, on a case-by-case basis.

The natural behavior of the MMSHC is that it will present higher AC voltage ripple at low-frequency operation. This is also the case for the MMC, which presents a typical submodule-capacitor voltage ripple with the components  $\omega$  and  $2\omega$ . The MMSHC operates switching alternately between the grid and the generator terminals, which means that current components with frequencies  $\omega_g$  and  $\omega_l$  (grid and load frequencies, respectively) will flow through the submodule capacitors causing a voltage ripple. Nonetheless, it is important to emphasize once again that wind-turbine applications do not require a low-frequency operation since the generator speed will be controlled to operate within a frequency range that does not include very low frequencies. Thus, a high voltage ripple should not occur in the MMSHC nor in the MMC in the wind-turbine application. It means that submodule capacitors with a relatively small capacitance values can be adopted in both converters. The M<sup>3</sup>C, on the other hand, presents reduced voltage ripple at low frequencies (which makes it an attractive solution for some machine drives) but it presents extremely high voltage ripple when its load-side frequency comes close to the grid-side frequency [12]. The M<sup>3</sup>C presents an unstable behavior when  $\omega_l = \omega_g$  [12], which is a situation that will commonly happen in a wind-turbine application. Thus, the usage of the M<sup>3</sup>C in a wind-turbine application can be quite tricky and challenging. At least, bigger capacitors should be

required for the M<sup>3</sup>C, in comparison to the MMC and to the MMSHC, because of its increased submodule-capacitor voltage ripple when  $\omega_l \approx \omega_g$ .

Another important characteristic of the MMSHC is the fact that it only requires three inductors at the connecting point of each converter phase and each grid phase (see Fig. 1). The MMC requires twelve arm inductors and the M<sup>3</sup>C requires nine string inductors. The arm/string inductors in the MMC and in the M<sup>3</sup>C have two main functions [27], [28]: to limit undesired AC circulating currents that increase the conduction losses and deteriorate the converter efficiency, and to limit overcurrents that occur due to internal faults, especially DC-side faults that represent a critical problem for MMCs built with HB submodules. One of the interesting characteristics of the MMSHC is the lack of circulating-current paths, which is a consequence of its topology in which different submodule strings are never connected, simultaneously, to the same terminal. In other words, each phase of the MMSHC is decoupled from the other two phases and is composed of two submodule strings that operate in a complementary fashion, meaning that these strings are never connected simultaneously to the same terminal. There is only one submodule string connected to any grid terminal and to any generator terminal at any time. In the MMC case (see Fig. 6) each leg is composed of two arms that are connected to the same terminal of the grid. Arm inductors are necessary because these two arms cannot be directly connected to the same terminal. In the M<sup>3</sup>C case (see Fig. 7), there are three different submodule strings connected to each phase of the grid and, thus, string inductors are required because the three submodule strings cannot be directly connected to the same terminal. Once again, the MMSHC only requires three inductors connected between each phase of the converter and each phase of the grid. These inductors are necessary to allow for the control of the current and power injected into the grid. The reduced capacitance and inductance requirements of the MMSHC can be considered as an important advantage in comparison to the MMC and the M<sup>3</sup>C, especially if these converters are used in applications that require lightness and compactness such as offshore wind turbines, i.e., these turbines are built on top of complex foundations that must be capable to support the turbine structure.

## V. SIMULATION RESULTS

In this section, simulation results will be presented based on the software PSCAD/EMTDC to demonstrate the basic operation and behavior of the MMSHC, as well as to demonstrate the performance of the converter in a machine-drive application representing a high-power wind turbine. In the first simulation analysis, the MMSHC will operate supplying power to a RL load and its load side will be controlled in an open-loop fashion synthesizing voltages with different frequencies and different amplitudes at the load terminals. In the second simulation analysis, the converter will operate driving a permanent-magnet synchronous generator (PMSG) representing the wind turbine, and the load-side control will be performed according to the FOC technique presented in Fig. 4. In both cases, however, the grid-side of the converter will be



controlled in a way as to regulate the submodule-capacitor voltages, while controlling the current injected into the grid (see control diagram presented in Fig. 4).

#### A. MMShC Supplying Power to a RL Load

As previously mentioned, the first simulation analysis is related to the operation of the MMShC supplying power to a RL load. In this simulation, the converter is connected to a 50-Hz, 5-kV grid and it supplies power to a RL load with the following parameters:  $L=10$  mH and  $R=25$   $\Omega$ . The MMShC is built with  $N = 5$  submodules per string and it has 5-mH inductors connected between each of its phases and each phase of the grid. This simulation aims to demonstrate the basic operation of the converter. Initially, the voltage synthesized at the load terminals presents amplitude equal to 5 kV and frequency equal to 50 Hz, and the submodule-capacitor voltages are regulated with a value equal to 1 kV. At  $t = 2.5$  s, the submodule-capacitor voltage reference increases to  $v_{dc}^* = 1.2$  kV. At  $t = 4$  s, the submodule-capacitor voltage reference goes back to  $v_{dc}^* = 1$  kV. At  $t = 6$  s, a new RL load ( $L=5$  mH and  $R=25$   $\Omega$ ) is connected to the load terminals. Initially, the switching frequency of the swap switches is equal to 50 Hz. At  $t = 8$  s, the switching frequency of the bidirectional-switch stacks (swap switches) increases to 150 Hz. Finally, at  $t = 10$  s, the frequency of the voltage synthesized at the load terminals changes to 20 Hz and its amplitude changes to 3.25 kV. The obtained simulation results are shown in Fig. 12, Fig. 13, and in Fig. 14. In Fig. 12(a), the multilevel 50-Hz voltages synthesized by the MMShC at the grid terminals are shown. In Fig. 12(b), the multilevel voltages synthesized by the MMShC at the load terminals are shown. As previously explained, initially, the converter is controlled to synthesize a 5-kV, 50-Hz voltage at the load terminals. At  $t = 10$  s, the converter starts to synthesize a 3.25-kV, 20-Hz voltage at the load terminals. These results demonstrate that the MMShC is capable to behave as a controlled voltage source. In Fig. 12(c), the grid-side power ( $P_g$ ) and load-side power ( $P_l$ ) of the MMShC are shown. The first thing that is important to notice is the fact that the grid-side and the load-side power remain with equal values, in steady state, throughout the entire simulation period. This is a consequence of the grid-side control that absorbs from the grid the power to be supplied to the load, while maintaining the submodule-capacitor voltages regulated according to the desired reference.

In Fig. 13(a) and (b), the MMShC's grid-side and load-side currents are shown, respectively. These are currents with a relatively high power quality (maximum of 5% of total harmonic distortion). An even higher power quality could be obtained if a higher number of levels was adopted in the converter. In this simulation analysis, the MMShC was modeled with only  $N = 5$  levels to limit the simulation time, which was already quite high. In a real application, a higher number of levels would be adopted, which would lead to currents with high power quality. It is important to highlight that the voltage synthesized by the MMShC is the typical staircase-shape voltage synthesized by any converter with a modular multilevel structure. This voltage comes closer to a

perfect sinusoidal signal the higher the number of levels in the submodule strings. Increasing the frequency of the LSC-PWM carriers would also contribute for an increased power quality of the MMShC's grid-side and load-side currents.

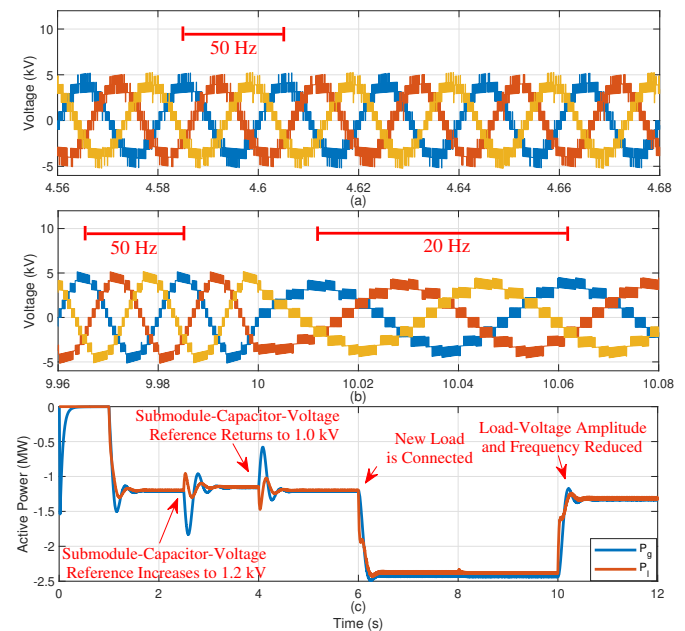


Fig. 12. Simulation results. (a) Voltages synthesized at grid terminals, (b) voltages synthesized at load terminals and (c) grid-side and load-side power.

In Fig. 14(a) and (b), the phase-A String-X submodule-capacitor voltages and the phase-A String-Y submodule-capacitor voltages are shown, respectively. As previously mentioned, at  $t = 2.5$  s, the submodule-capacitor voltage reference changes from 1 kV to 1.2 kV. This fact obviously imposes an oscillation to the grid-side and load-side power values as shown in Fig. 12(c). By observing Fig. 14(a) and (b), it is possible to notice that the proposed control is capable to regulate the submodule-capacitor voltages of both strings according to the provided reference ( $v_{dc}^* = 1.2$  kV). At  $t = 4$  s, the submodule-capacitor voltage reference goes back to 1 kV, and the proposed control is capable once again to track this reference as shown in Fig. 14(a) and (b). This variation is once again reflected in oscillations in the grid-side and load-side power as shown in Fig. 12(c).

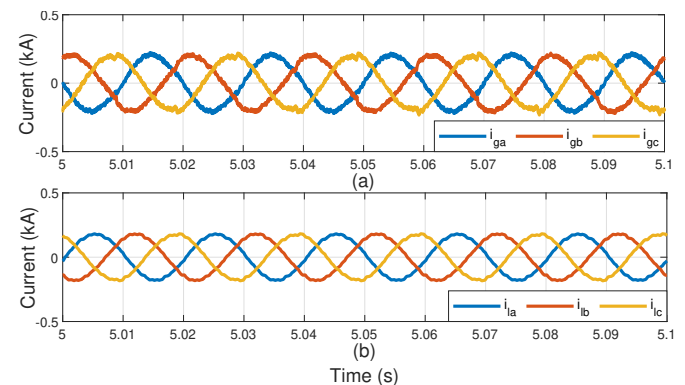


Fig. 13. Simulation results. (a) Grid-side currents, and (b) load-side currents.

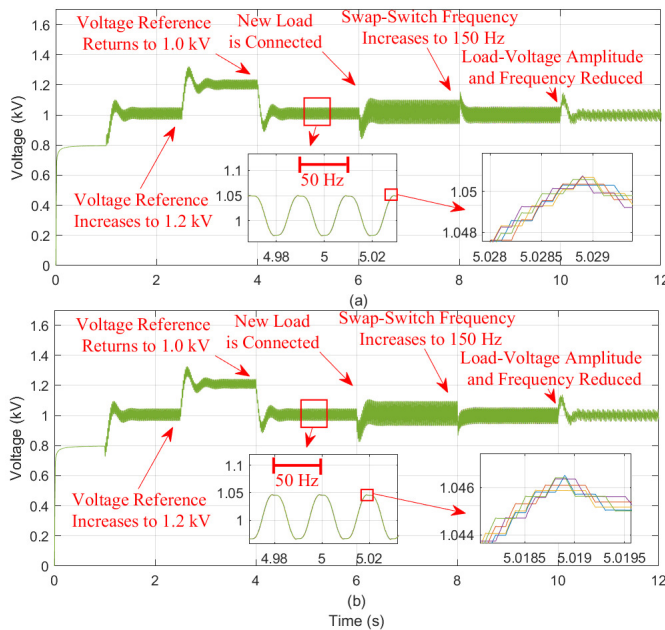


Fig. 14. Simulation results. (a) MMShC phase-A String-X submodule-capacitor voltages and (b) phase-A String-Y submodule-capacitor voltages.

At  $t = 6$  s, the new load is connected, which leads to an increase of the grid-side and load-side power values as shown in Fig. 12(c). The connection of the new load represents a disturbance to the submodule-capacitor voltage control as shown in Fig. 14(a) and (b). Nonetheless, the proposed control technique is capable to maintain the submodule-capacitor voltages regulated according to the reference  $v_{dc}^* = 1$  kV. By observing the zoom in the submodule-capacitor voltages, a 50-Hz ripple can be noticed. This is a consequence of the 50-Hz switching frequency of the bidirectional-switch stacks that connect each submodule string to the grid terminal (charging mode in this case) and to the load terminal (discharging mode in this case) in an alternate fashion. This ripple is referred to as swapping ripple and it will be further explained in the experimental result section of this paper. A deeper zoom in the submodule-capacitor voltages (see Fig. 14(a) and (b)) shows the voltages of the capacitors of each individual submodule within the given string. These voltages present similar values due to the sorting algorithm responsible for the submodule-capacitor voltage balancing. It is interesting to notice that the submodule-capacitor voltage ripple increases when the new load is connected at  $t = 6$  s. Since the power supplied to the load increases (and, thus, the power absorbed from the grid increases as well), then the submodule capacitors will be charged/discharged faster because the switching frequency of the bidirectional-switch stacks is kept fixed. At  $t = 8$  s, though, the switching frequency of the bidirectional-switch stacks increases to 150 Hz, and, thus, the submodule-capacitor-voltage swapping ripple is reduced, i.e., the submodule strings switch between the charging and discharging terminals with a higher frequency, which means that they are less charged/discharged before they are connected to the opposite terminal. Finally, at  $t = 10$  s, both the amplitude and the frequency of the voltage synthesized by

the MMShC at the load terminals are reduced, as previously mentioned, which results in a reduced power being supplied to the RL load. This fact can be noticed by observing Fig. 12(c). In Fig. 14(a) and (b), it is possible to notice that the variation in the load power represents a disturbance to the control of the submodule-capacitor voltages, but the proposed control is once again capable to maintain the capacitor voltages regulated in steady state. Another important issue to observe in this simulation analysis is that the MMShC is capable to operate in a stable and low-voltage-ripple fashion when the frequency of its grid-side voltage is equal to the frequency of its load-side voltage ( $f_g = f_l = 50$  Hz). This is an advantage in comparison to the  $M^3C$ .

### B. MMShC Driving PMSG-Based Wind Turbine

The second simulation corresponds to the analysis of the MMShC operation while driving a PMSG, which represents the wind-turbine generator. In this simulation, the converter is connected to a 50-Hz, 5-kV grid and it drives a PMSG with rated power, voltage and frequency equal to 3 MVA, 5 kV and 60 Hz. The MMShC is built with  $N = 5$  submodules per string and it has 5-mH inductors connected between each of its phases and each phase of the grid. In this analysis, the grid-side of the MMShC is once again controlled through the method shown in Fig. 4.

The obtained simulation results are shown in Fig. 15 and Fig. 16. In Fig. 15(a), the multilevel voltages synthesized by the MMShC at the grid terminals are illustrated, which are 50-Hz signals. In Fig. 15(b), the multilevel voltages synthesized by the MMShC at the generator terminals are shown. As previously mentioned, these voltages are a consequence of the generator control aiming to regulate the machine speed. At  $t = 1$  s, the system is started and the speed reference is set to a value equal to  $\omega^* = 0.22$  pu. At  $t = 3$  s, the generator speed reference is increased to 0.25 pu. The voltages shown in Fig. 15(b) are 15-Hz signals since, in the given period, the generator speed is equal to 0.25 pu and since the machine rated frequency is equal to 60 Hz. In Fig. 15(c), the generator angular speed is shown, and it is possible to notice that the proposed control applied to the MMShC is capable to regulate the generator speed according to the mentioned reference. At  $t = 6$  s, the wind speed is increased, which results in a higher power value produced by the turbine. In Fig. 15(d), the power absorbed from the turbine by the MMShC ( $P_l$ ) and the power injected into the grid by the converter ( $P_g$ ) are shown. Once again, the power injected into the grid by the converter is kept equal to the power absorbed from the turbine, in steady state, which is a consequence of the grid-side control aiming at regulating the submodule-capacitor voltages.

In Fig. 16(a) and (b), the MMShC phase-A String-X submodule-capacitor voltages and phase-A String-Y submodule-capacitor voltages are shown, respectively. These signals are kept regulated with the desired voltage value equal to 1 kV throughout the entire simulation period. Besides, the zoom in the submodule-capacitor-voltage signals illustrate once again the effectiveness of the sorting algorithm responsible for maintaining all the capacitors within the same submodule string with similar voltage values.

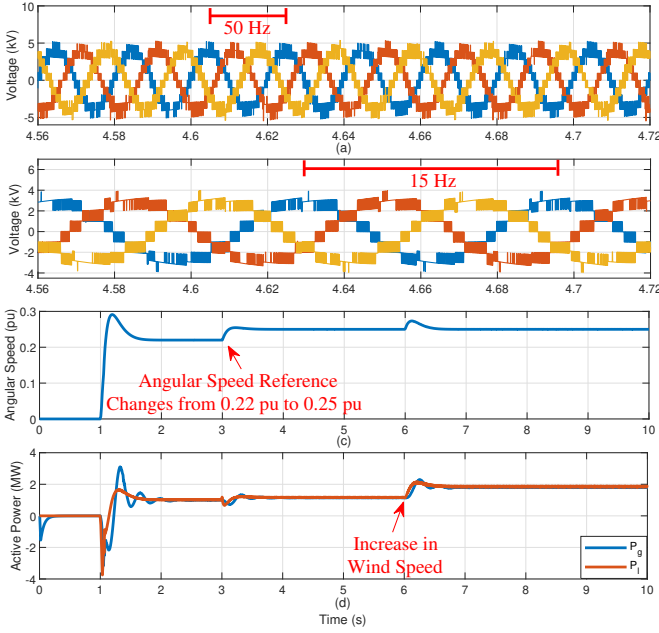


Fig. 15. Simulation results. (a) Voltages synthesized by the MMSHC at the grid terminals, (b) voltages synthesized by the MMSHC at the generator terminals, (c) machine angular speed and (d) grid-side and generator-side power.

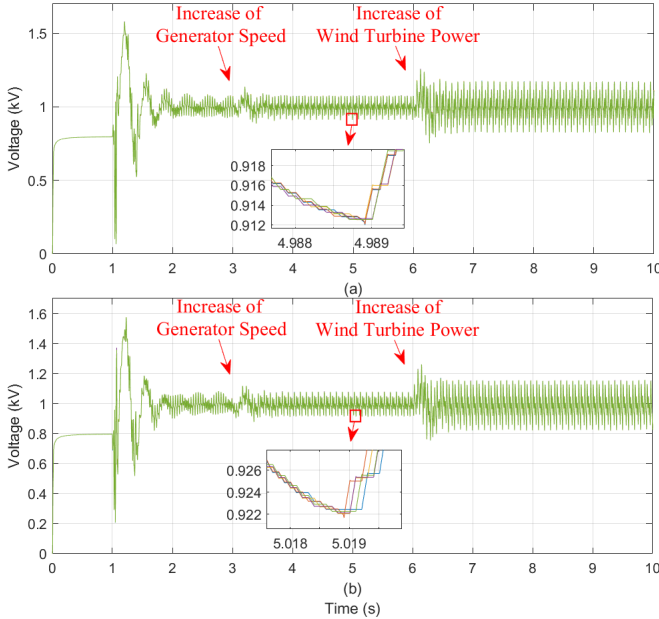


Fig. 16. Simulation results. (a) MMSHC phase-A String-X submodule-capacitor voltages and (b) MMSHC phase-A String-Y submodule-capacitor voltages.

## VI. EXPERIMENTAL VALIDATION

In this section, experimental results obtained through a low-scale prototype will be presented. The built prototype is shown in Fig. 17 and it is a single-phase version of the proposed converter solution. The hardware is composed of two strings with  $N = 3$  FB submodules (String X and String Y) based on IGBTs. Each submodule has a  $C = 16$ -mF capacitor integrated. Four bidirectional switches are also part of the built hardware and two of these switches form one swap circuit resulting in Swap 1 and Swap 2. A Texas Instruments

TMS320F28379D digital-signal processor (DSP) was used to control the converter. A  $L_g = L_t = 5$ -mH inductor was connected to both grid and load terminals of the converter. The hardware was connected to an AC power supply that emulated a  $V_g = 50$ -V,  $f_g = 50$ -Hz AC grid, and the converter supplied power to a load resistor ( $R_l = 16$  m $\Omega$ ). In this experimental test, the grid side of the MMSHC was controlled according to the method presented in Fig. 4, aiming to regulate the submodule-capacitor voltages while absorbing power from the grid. The submodule-capacitor voltages were regulated with an average value equal to  $v_{cap}^* = 23$  V, where the symbol \* indicates a control reference. The load side of the converter, on the other hand, was controlled in an open-loop fashion synthesizing a  $V_l^* = 50$ -V,  $f_l^* = 20$ -Hz voltage. The internal control of the MMSHC was implemented according to the algorithm described in Fig. 5. The switching frequency of the swap circuit (bidirectional switches) was kept fixed with a value equal to  $f_{BS} = 20$  Hz. The test setup parameters are summarized in TABLE IV.

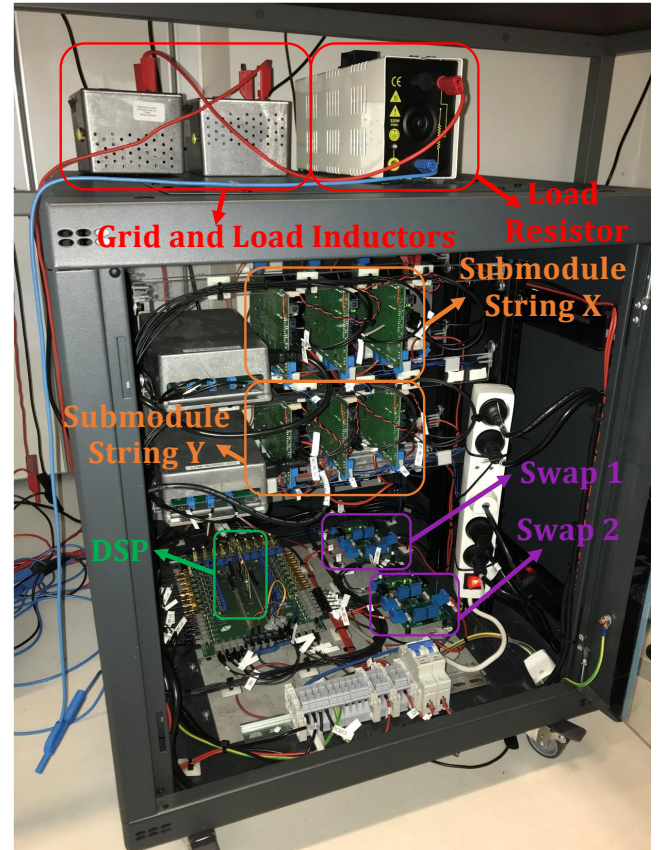


Fig. 17. MMSHC low-scale test setup.

The collected experimental results are shown in Fig. 18, Fig. 19, Fig. 20 and Fig. 21. In the first, second, third and fourth sub figures of Fig. 18, the load-side voltage, load-side current, grid-side voltage and grid-side current of the converter are shown, respectively. These results demonstrate that the proposed converter is capable to synthesize staircase-shape multilevel voltages with different frequencies at its two terminals. This would be the case in a WT application in which the grid-side frequency is fixed by the grid and the generator-side frequency varies to control the machine



speed. In Fig. 19, the String-X submodule-capacitor voltages are shown and one can notice that the proposed control is capable to regulate the average value of the capacitor voltages according to the given reference. In this figure, the 20-Hz ripple in the voltage signals can be observed, which is a consequence of the switching frequency of the bidirectional switches. Once again, it is important to notice that these switches can operate with this extremely low frequency in the proposed topology. In Fig. 20 and Fig. 21, a closer view in the String-X submodule-capacitor voltages and String-Y submodule-capacitor voltages, respectively, is shown by using an AC coupling in the oscilloscope. In these figures, the three individual voltages of each capacitor in each submodule string can be seen. It is important to notice that the three submodule capacitors within the same string remain with similar voltage values due to the sorting algorithm (see Fig. 5), responsible for the submodule-capacitor voltage balancing. These results validate the internal control of the proposed MMSHC.

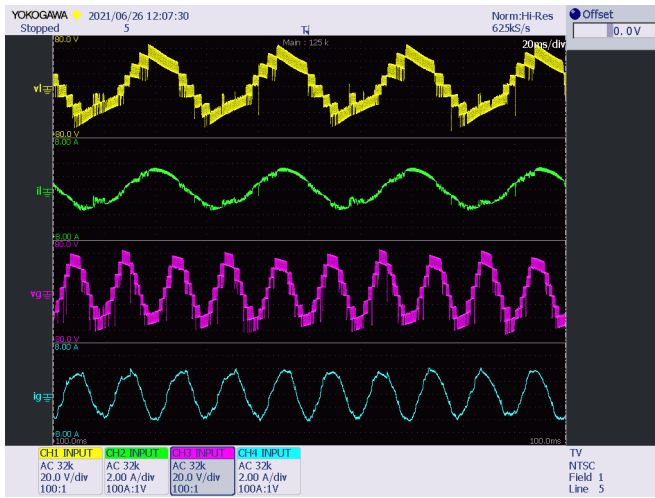


Fig. 18. Experimental results. The first sub figure (upper one) shown the load-side voltage, the second sub figure shows the load-side current, the third sub figure shows the grid-side voltage and the fourth sub figure shows the grid-side current.

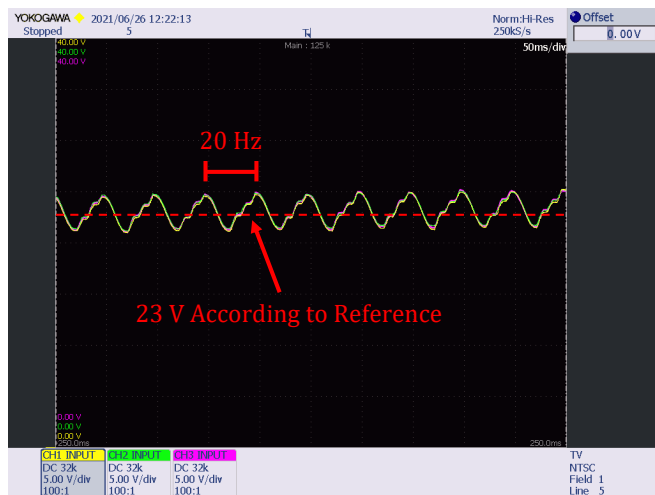


Fig. 19. Experimental results. String-X submodule-capacitor voltages.

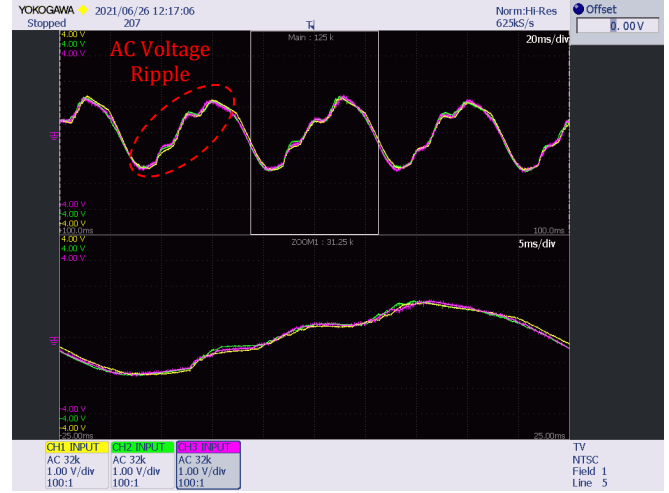


Fig. 20. Experimental results. AC coupling of String-X submodule-capacitor voltages.

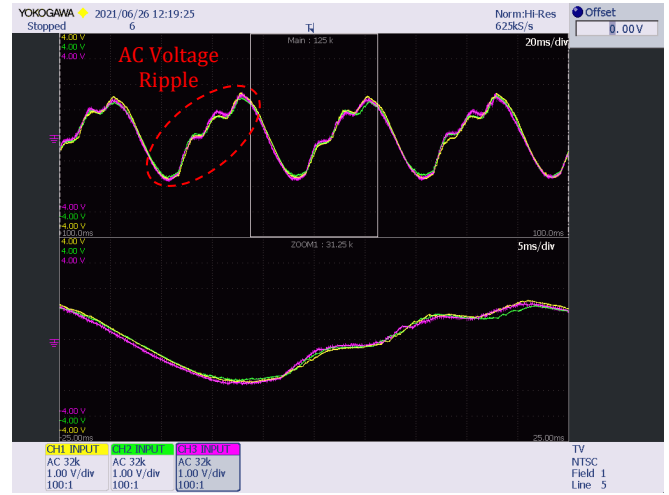


Fig. 21. Experimental results. AC coupling of String-Y submodule-capacitor voltages.

TABLE IV  
EXPERIMENTAL PROTOTYPE PARAMETERS.

MMSHC Parameters	
Parameter	Value
$N$	3
$C$	16 mF
$L_g$	5 mH
$f_{BS}$	20 Hz
$v_{cap}^*$	23 V
Load Parameters	
Parameter	Value
$L_l$	5 mH
$R_l$	16 mΩ
$V_l^*$	50 V
$f_l^*$	20 Hz
AC Power Supply Parameters	
Parameter	Value
$V_g$	50 V
$f_g$	50 Hz

The experimental results presented in this paper demonstrate some important features of the proposed MMSHC in comparison to other converter topologies well-established in the industry. For example, these results show that the MMSHC is capable to synthesize a multilevel staircase-shape voltage, with a relatively high power quality, which can easily be filtered out. This voltage profile can even be improved if a higher number of levels is adopted in the converter solution, which would be something straightforward to do because of the modularity and scalability of the submodule strings. This is a special feature common to all the converter topologies with a modular multilevel structure such as the MMC and the  $M^3C$ . The possibility of synthesizing the multilevel AC voltage is an important advantage in comparison to TL and NPC converters since this voltage profile is easier to be filtered out in terms of both harmonic content and  $\frac{dv}{dt}$ .

Another important feature of the MMSHC demonstrated through the experimental results is the operation of the swap circuit. The submodule-capacitor voltages shown in Fig. 19, Fig. 20 and Fig. 21 are capable to illustrate important characteristics of the capacitor voltage ripple. Besides having an average value, which is regulated by the control with 23 V in these experimental results, the MMSHC submodule-capacitor voltage is also composed of two different ripple components. The first is an AC component, which is a consequence of the AC currents flowing through the submodule strings. As previously explained, the AC component of the submodule-capacitor voltage ripple is the same as in a SSBC converter that presents a typical  $2\omega$  submodule-capacitor voltage ripple, in which  $\omega$  corresponds to the frequency of the AC current flowing through the submodule string. Since the submodule strings of the MMSHC can be connected to both grid and load terminals, then the AC submodule-capacitor voltage ripple will depend on the frequency of the terminal to which the string is connected. The second voltage ripple component is what can be referred to as a swapping component, i.e., in the MMSHC, when one of its strings is connected to a load, its submodule capacitors are continuously discharged supplying power to this load. In this case, a decreasing DC component appears in the submodule-capacitor voltages. When the string is then connected to the grid, its submodule capacitors are continuously charged and, then an increasing DC component appears in the submodule-capacitor voltages. The swapping voltage ripple is a function of the switching frequency of the bidirectional switches that are responsible for alternating the connection of the submodule strings between the load and the grid/source terminals. By observing the experimental results shown in Fig. 19, Fig. 20 and Fig. 21, it is possible to notice the presence of the 20-Hz swapping voltage ripple (because of the 20-Hz switching frequency of the bidirectional switches), and the smaller AC ripple that occurs in between the 20-Hz switching operation. Once again, in this experimental test, the bidirectional switches of the swap circuit operated with 20 Hz, which is an extremely low switching frequency for a semiconductor device. The possibility of operating the swap switches with a low switching frequency will be extremely important when a large-scale medium-voltage converter is developed, in which the swap circuit will have to be built

with series-connected semiconductor devices. The low switching frequency of the MMSHC bidirectional-switch stacks is an important advantage compared to the TL and the NPC converters that must operate with a high switching frequency, resulting in poor reliability and poor efficiency for their stacks of series-connected semiconductor devices. The switching frequency of the MMSHC swap circuit should be defined according to how fast its submodule capacitors are charged and discharged, which depends on the size of these capacitors and on the power handled by the converter. Then, it would be reasonable to expect that, in a large-scale solution, the switching frequency of the swap switches would have to be increased since increasing the size of the capacitors in not an attractive option. Nonetheless, it is important to highlight that a capacitor's energy is calculated as  $E_c = \frac{1}{2}CV^2$ , which means that the energy stored in it increases with the square of its voltage. Thus, for higher voltage levels, which will be the case in a large-scale MMSHC, considerably more energy will be stored in the converter's submodule capacitors, which will lead to slower charging/discharging cycles of these capacitors, contributing for the possibility of operating the swap switches with a low switching frequency.

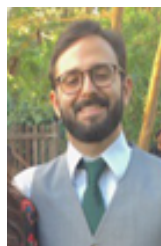
## VII. CONCLUSION

This paper introduced the MMSHC version with capacitors only, which could be a promising converter solution to drive modern/future high-power medium-voltage WTs. In this paper, a control technique is proposed to control the grid side of the converter in order to regulate its submodule-capacitor voltages while injecting power into the grid. Moreover, a comparative analysis with other well-established converter solutions was presented in terms of power ratings of semiconductor devices and in terms of submodule/capacitor count. This analysis concluded that, even though the proposed solution presents an increased requirement in semiconductor device power, it presents a considerably reduced submodule, capacitor and inductor count, which could lead to advantages in terms of weight, volume and costs. In this paper, simulation results were presented demonstrating the basic operation of the MMSHC with the proposed control technique and demonstrating the effectiveness of the converter in driving an electrical machine representing the WT generator. The simulation results proved that the proposed grid-side control is capable to maintain the submodule-capacitor voltages of the converter regulated in every tested conditions. Moreover, the simulation results proved that the proposed topology was capable to regulate the generator speed while injecting the produced power into the grid. Finally, experimental results in a low-scale prototype were presented validating important aspects of the proposed converter solution such as its grid-side control, its internal control and sorting algorithm, the ability of the converter in synthesizing different voltages with different frequencies at its two terminals, and the operation of the swap circuit.

## REFERENCES

- [1] ABB, *PCS 6000 for large wind turbines Medium voltage, full power converters up to 9 MVA*, 2012. [Online]. Available: <https://new.abb.com/docs/default-source/ewea-doc/pcs6000wind.pdf?sfvrsn=2>

- [2] M. Diaz, R. Cárdenas, M. Espinoza, A. Mora, and P. Wheeler, "Modelling and control of the modular multilevel matrix converter and its application to wind energy conversion systems," in *IECON 2016 - 42nd Annual Conference of the IEEE Industrial Electronics Society*, Florence, 2016.
- [3] V. Yaramasu, B. Wu, P. C. Sen, S. Kouro, and M. Narimani, "High-power wind energy conversion systems: State-of-the-art and emerging technologies," *Proceedings of the IEEE*, vol. 103, no. 5, pp. 740–788, 2015.
- [4] A. Madariaga, J. L. Martín, I. Zamora, I. Martínez De Alegría, and S. Ceballos, "Technological trends in electric topologies for offshore wind power plants," *Renewable and Sustainable Energy Reviews*, vol. 24, pp. 32–44, 2013.
- [5] N. Fichaux, J. Beurskens, P. H. Jensen, J. Wilkes, S. Frandsen, J. D. Sorensen, P. Eecen, C. Malamatenios, J. A. Gomez, J. Hemmelmann, G. van Kuik, B. Bulder, F. Rasmussen, B. Janssen, T. Fischer, E. Bossanyi, M. Courtney, J. Giebhardt, R. Barthelmie, O. Holmstrom, D. Iuga, and S. Wokke, *UPWIND - Design Limits and Solutions for Very Large Wind Turbines*. Tech. Rep. The European Wind Energy Association; Brussels, Belgium, 2011.
- [6] M. Diaz, R. Cardenas, M. Espinoza, F. Rojas, A. Mora, J. C. Clare, and P. Wheeler, "Control of Wind Energy Conversion Systems Based on the Modular Multilevel Matrix Converter," *IEEE Transactions on Industrial Electronics*, vol. 64, no. 11, pp. 8799–8810, 2017.
- [7] F. V. Robinson and V. Hamidi, "Series connecting devices for high-voltage power conversion," *42nd International Universities Power Engineering Conference*, 2007.
- [8] K. Sharifabadi, L. Harnefors, H.-P. Nee, S. Norrga, and R. Teodorescu, *Design, Control, and Application of Modular Multilevel Converters for HVDC Transmission Systems*. John Wiley & Sons, 2016.
- [9] P. Sun, Y. Tian, J. Pou, and G. Konstantinou, "Beyond the MMC : Extended Modular Multilevel Converter Topologies and Applications," *IEEE Open Journal of Power Electronics*, vol. Early Access, 2022.
- [10] M. Soares and E. H. Watanabe, "MMC Applied to Pumped Hydro Storage using a Differentiable Approximation of a Square Wave as Common-Mode Voltage during Low-Frequency Operation," *2020 IEEE 21st Workshop on Control and Modeling for Power Electronics, COMPEL 2020*, 2020.
- [11] M. Hagiwara, I. Hasegawa, and H. Akagi, "Start-up and low-speed operation of an electric motor driven by a modular multilevel cascade inverter," *IEEE Transactions on Industry Applications*, vol. 49, no. 4, pp. 1556–1565, 2013.
- [12] M. Diaz, R. C. Dobson, E. Ibacetia, A. Mora, M. Urrutia, M. Espinoza, F. Rojas, and P. Wheeler, "An overview of applications of the modular multilevel matrix converter," *Energies*, vol. 13, no. 21, pp. 1–37, 2020.
- [13] B. Fan, K. Wang, P. Wheeler, C. Gu, and Y. Li, "A Branch Current Reallocation Based Energy Balancing Strategy for the Modular Multilevel Matrix Converter Operating Around Equal Frequency," *IEEE Transactions on Power Electronics*, vol. 33, no. 2, pp. 1105–1117, 2018.
- [14] W. Kawamura and H. Akagi, "Control of the modular multilevel cascade converter based on triple-star bridge-cells (MMCC-TSBC) for motor drives," *2012 IEEE Energy Conversion Congress and Exposition, ECCE 2012*, pp. 3506–3513, 2012.
- [15] W. Kawamura, M. Hagiwara, and H. Akagi, "Control and experiment of a modular multilevel cascade converter based on triple-star bridge cells," *IEEE Transactions on Industry Applications*, vol. 50, no. 5, pp. 3536–3548, 2014.
- [16] W. Kawamura, K.-L. Chen, M. Hagiwara, and H. Akagi, "A Low-Speed, High-Torque Motor Drive Using a Modular Multilevel Cascade Converter Based on Triple-Star Bridge Cells (MMCC-TSBC)," *IEEE Transactions on Industry Applications*, vol. 51, no. 5, pp. 3965 – 3974, 2015.
- [17] B. Wu, Y. Lang, N. Zargari, and S. Kouro, *Power Conversion and Control Of Wind Energy Systems*. John Wiley & Sons, 2011.
- [18] D. Sera, L. Mathe, and M. Ricco, "Flexible and efficient switched string converter," International Patent - World Intellectual Property Organization/Patent Cooperation Treaty (WIPO/PCT) WO 2020/043 258 A1, Mar. 05, 2020.
- [19] G. F. Gontijo, T. Kerekes, D. Sera, M. Ricco, L. Mathe, and R. Teodorescu, "Medium-Voltage Converter Solution with Modular Multilevel Structure and Decentralized Energy Storage Integration for High-Power Wind Turbines," *IEEE Transactions on Power Electronics*, vol. 36, no. 11, pp. 12 954–12 967, 2021.
- [20] G. F. Gontijo, D. Sera, M. Ricco, L. Mathe, T. Kerekes, and R. Teodorescu, "Dispatchable High-Power Wind Turbine based on a Multilevel Converter with Modular Structure and Hybrid Energy Storage Integration," *IEEE Access*, vol. 9, pp. 1–1, 2021.
- [21] H. Akagi, S. Inoue, and T. Yoshii, "Control and performance of a transformerless cascade PWM STATCOM with star configuration," *IEEE Transactions on Industry Applications*, vol. 43, no. 4, pp. 1041–1049, 2007.
- [22] J. I. Ota, Y. Shibano, N. Niimura, and H. Akagi, "A phase-shifted-PWM D-STATCOM using a modular multilevel cascade converter (SSBC) - Part I: Modeling, analysis, and design of current control," *IEEE Transactions on Industry Applications*, vol. 51, no. 1, pp. 279–288, 2015.
- [23] H. Akagi, "Classification, terminology, and application of the modular multilevel cascade converter (MMCC)," *IEEE Transactions on Power Electronics*, vol. 26, no. 11, pp. 3119–3130, 2011.
- [24] P. Wheeler, J. Rodriguez, J. C. Clare, L. Empringham, and A. Weinstein, "Matrix Converters : A Technology Review," *IEEE Transactions on Industrial Electronics*, vol. 49, no. 2, 2002.
- [25] Z. Malekjamshidi, M. Jafari, J. Zhang, and J. Zhu, "Design and Analysis of Protection Circuits for Safe Operation of Direct Matrix Converters," *2017 20th International Conference on Electrical Machines and Systems, ICEMS 2017*, pp. 0–3, 2017.
- [26] M. M. Merlin and T. C. Green, "Cell capacitor sizing in multilevel converters: Cases of the modular multilevel converter and alternate arm converter," *IET Power Electronics*, vol. 8, no. 3, pp. 350–360, 2015.
- [27] Q. Tu, Z. Xu, H. Huang, and J. Zhang, "Parameter design principle of the arm inductor in modular multilevel converter based HVDC," *2010 International Conference on Power System Technology: Technological Innovations Making Power Grid Smarter, POWERCON2010*, pp. 0–5, 2010.
- [28] S. Du, A. Dekka, B. Wu, and N. Zargari, "Modular Multilevel Converters Analysis, Control and Applications," in *IEEE Press*, 2018.



**Gustavo F. Gontijo** (Member, IEEE) received the B.Sc. and M.Sc. degrees in electrical engineering from the Federal University of Rio de Janeiro (UFRJ), Rio de Janeiro, Brazil, in 2016 and 2018, respectively. He is currently pursuing the Ph.D. degree with AAU Energy, Aalborg University, Aalborg Ost, Denmark.

From 2014 to 2015, he was an Intern with the Leopoldo Americo Miguez de Mello Research and Development Center (Cenpes) of the Brazilian energy company Petrobras, where he was involved with research works related to solar photovoltaic systems and wind turbines. From 2015 to 2019, he was with the Laboratory of Power Electronics and Medium Voltage Applications, which is part of the Alberto Luiz Coimbra Institute for Graduate Studies and Research in Engineering (LEMT/COPPE/UFRJ). In LEMT, he was involved in research works related to power electronics applied to wind turbines, STATCOMs, active filters, virtual synchronous machines, and microgrids. From 2020 to 2021, he was a Research Assistant with AAU Energy, Aalborg University. From 2021 to 2022, he was a Guest Researcher with Ørsted Wind Power A/S, Gentofte, Denmark, working in a research collaboration with the title "Eigenvalue-Based Stability Assessment of an Off-shore Wind Power Plant with an MMC-Based HVDC Connection". Recently, he joined Ørsted Wind Power A/S as a Power System Engineer. His current research interests include modular multilevel converter solutions with and without energy storage integration for medium-voltage applications, stability of power-electronic-based power systems, and modern HVDC transmission systems based on the modular multilevel converter.



**Tamas Kerekes** (Senior Member, IEEE) obtained an Electrical Engineer diploma in 2002 from Technical University of Cluj, Romania, with specialization in Electric Drives and Robots. In 2005, he graduated the Master of Science program at Aalborg University, Institute of Energy Technology in the field of Power Electronics and Drives. In 2009 obtained the PhD degree from the Institute of Energy Technology, Aalborg University. The topic of the PhD program was: "Analysis and modeling of transformerless PV inverter systems".

Currently he is employed at Aalborg University as an Associate professor and is doing research within the field of grid connected renewable energy systems with focus on topologies and control of power electronic converters.





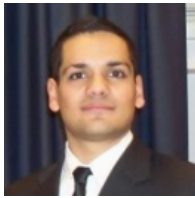
**Dezso Sera** (Senior Member, IEEE) received his B.Sc. and M.Sc. degrees in Electrical Engineering from the Technical University of Cluj, Romania in 2001 and 2002, respectively; MSc in Power Electronics and PhD on PV systems from Aalborg University, Denmark, Department of Energy Technology, in 2005 and 2008, respectively. In the period of 2009-2019 he was the leader of the Photovoltaic Systems Research Programme at the same department.

Since 2020, he is with Queensland University of Technology, where he serves as deputy director for the Centre for Clean Energy Technologies and Practices. His research interests include modelling, characterisation, diagnostics and maximum power point tracking (MPPT) of PV arrays, as well as power electronics, and grid and energy storage integration for PV systems.



**Remus Teodorescu** (Fellow, IEEE) received the Dipl.Ing. degree in electrical engineering from the Politehnica University of Bucharest, Romania, in 1989, and the PhD. degree in power electronics from the University of Galati, Romania, in 1994.

In 1998, he joined AAU Energy, Aalborg University, power electronics section, where he currently works as a Full Professor. From 2013 to 2017, he was a Visiting Professor with Chalmers University of Technology, Sweden. He has coauthored the books *Grid Converters for Photovoltaic and Wind Power Systems* (Wiley-IEEE Press, 2011) and *Design, Control and Application of Modular Multilevel Converters for HVDC Transmission Systems* (Wiley-IEEE Press, 2016). He has coauthored over 500 IEEE journal and conference papers. His research interests include design and control of grid connected converters for photovoltaic and wind power systems, HVDC/FACTS based on MMC, SiC-based converters, storage systems for utility based on Li-Ion battery technology, and battery lifetime model using artificial intelligence. In 2021, he was awarded the Villum Investigator grant for the development of the Center of Research on Smart Battery at Aalborg University.



**Mattia Ricco** (Senior Member, IEEE) received the master's degree (cum laude) in electronic engineering from the University of Salerno, Fisciano, Italy, in 2011, and the Ph.D. double degree in electrical and electronic engineering from the University of Cergy-Pontoise, Cergy-Pontoise, France, and in information engineering from the University of Salerno in 2015.

From 2015 to 2018, he was a Postdoctoral Research Fellow with the Department of Energy Technology, Aalborg University, Denmark. From 2018 to 2021, he was a Senior Assistant Professor (Tenure Track) and since 2021 Associate Professor with the Department of Electrical, Electronic, and Information Engineering, University of Bologna, Bologna, Italy. His research interests include modular multilevel converters, battery management system, electric vehicle chargers, field-programmable gate array-based controllers, identification algorithms for power electronics, and photovoltaic systems.



**Laszlo Mathe** (Senior Member, IEEE) received the B.Sc. degree and the M.Sc. degree in electrical engineering from the Technical University of Cluj-Napoca, Cluj-Napoca, Romania, in 2000 and 2002, respectively, and the Ph.D. degree in electrical engineering from AAU Energy, Aalborg University, Aalborg, Denmark, in 2010. Between 2002 and 2007, he worked for the industry as a Control Development Engineer, while between 2007-2017 he worked as: Ph.D fellow, Assistant and finally as Associate Professor at Aalborg University. Since 2017, he has

been working as a Motor Control Expert at Robert Bosch company. His current research interests include control and design of power converters, control of electrical drives, photovoltaic systems, modulation techniques (MMC, two level inverters), vehicle electrification.